Laser & Photon. Rev. **2**, No. 3, 182–202 (2008) / **DOI** 10.1002/lpor.200710030

Abstract This paper reviews the theoretical analysis of light propagation we have carried out on multimode multi-step index (MSI) optical fibres. Starting from the Eikonal equation, we derive the analytical expressions that allow calculating the ray trajectories inside these fibres. We also analyse the effects of leaky rays on the transmission properties of MSI fibres. For this purpose, a single analytical expression for the evaluation of the ray power transmission coefficient is calculated. Afterwards, we investigate the effects of extrinsic and intrinsic coupling losses on the performance of MSI fibres, providing analytical expressions to calculate the coupling loss and, also, determining the most critical parameters. Finally, we carry out a comprehensive numerical analysis of the fibre bandwidth under different source configurations.

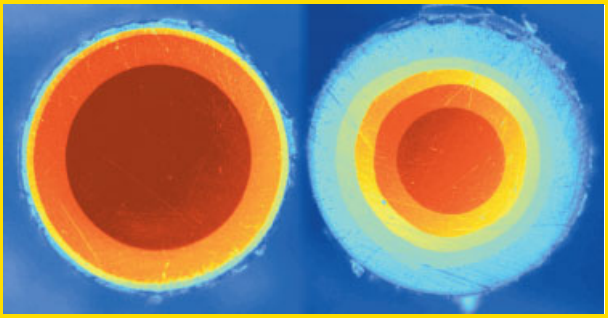

Cross-section photographs of two different MSI-POFs (left: Eska-Miu fibre; right: TVER fibre).

© 2008 by WILEY-VCH Verlag GmbH & Co. KGaA, Weinheim

Light propagation in multi-step index optical fibres

Joseba Zubia[*], *Gotzon Aldabaldetreku, Gaizka Durana, Jon Arrue, and Felipe Jiménez*

University of the Basque Country, Alda. Urquijo s/n, 48013 Bilbao, Spain

Received: 1 November 2007, Revised: 18 February 2008, Accepted: 27 February 2008
Published online: 26 March 2008

Key words: geometric optics; ray-tracing; MSI (multi-step index) optical fibres; polymer optical fibres

PACS: 42.15.-i, 42.15.Dp, 42.25.Gy, 42.81.-i

1. Introduction

During the last decades glass optical fibres have been widely used for transmitting information to very long distances at very high data rates [1, 2]. Simultaneously, researchers have been experimenting with other materials instead of the usual glass, in search of cheaper alternatives that might lead to similar performances. In this respect, polymer optical fibres (POFs) have been regarded as the most suitable choice, because they are easy to handle, flexible, and economical, although they are not used for very long distances because of their relatively high attenuation [3–5]. These characteristics make POFs especially suitable for short-haul communications links, where distances to cover are generally less than one kilometre.

The development of low-attenuation perfluorinated graded-index (GI) polymer optical fibres (GI-POFs) by professor Koike at Keio University [6–9], which surpass the capacity of the so far developed step-index (SI) polymer optical fibres (SI-POFs), has given rise to a great deal of applications and new technologies involving the employment of POFs [10, 11]. This fact has motivated Mitsubishi Rayon Co., Ltd. [12] and researchers at the University of TVER [13] to develop new prototypes corresponding to another variant of POFs, namely the multi-step index (MSI) polymer optical fibre (MSI-POF). MSI-POFs are intended to offer the same advantages of GI-POFs while maintaining the manufacturing costs sufficiently low [14, 15]. This is achieved due to the simpler processes involved in the manufacture of these types of fibres, as well as to the better stability of their refractive index profiles with ageing, temperature fluctuations and humidity changes. As a consequence, MSI-POFs combine the manufacturing simplicity of their SI counterparts and the higher bandwidths achievable with GI fibres. For instance, an MSI-POF of three layers with a numerical aperture (NA) of 0.25 allows bandwidths as high as 250 MHz · 100 m, thus complying with the IEEE1394/S400 specification [12, 14]. To date, the only available MSI-POFs are highly multimode, so we have only considered multimode MSI fibres, putting special emphasis on poly-methyl-methacrylate (PMMA) based POFs.

Corresponding author: e-mail: joseba.zubia@ehu.es

WILEY InterScience DISCOVER SOMETHING GREAT

© 2008 by WILEY-VCH Verlag GmbH & Co. KGaA, Weinheim

With the aim of clarifying some of the theoretical aspects regarding the performance of MSI fibres, we have carried out a comprehensive analysis of light propagation properties in such fibres using geometric optics. The main purpose of this review is, therefore, to report on the obtained theoretical results, whose validity has been corroborated by several experimental measurements and numerical simulations [16–18]. Our study begins with the derivation of the ray invariants which allow us to discuss the characteristics of the ray trajectory and set the classification of rays into bound, refracting and tunnelling categories. We also calculate a single analytical expression of the power transmission coefficient for both tunnelling and refracting rays. Afterwards, we carry out an analysis of both extrinsic and intrinsic coupling losses in MSI fibres. In the former case, we study the three fundamental types of mechanical misalignments between fibres, namely, longitudinal separation, axial or transverse offset, and angular misalignment. In the latter case, we investigate the effects of tolerances to each waveguide parameter that take place in standard manufacturing processes. In addition, we carry out a numerical analysis of pulse dispersion and bandwidth in MSI fibres under different light source configurations. Finally, we summarize the main conclusions derived from this work.

2. Ray propagation using geometric optics

The description of the light propagation in the MSI fibres analysed here is very simple, because their multimode behaviour enables us to adopt the classical geometric optics approach, replacing the concept of mode used in the electromagnetic theory of light by the concept of ray [19, 20]. Therefore, the most direct and conceptually simple way to describe the propagation of light in MSI fibres is by *tracing rays* along the fibre core. Ray propagation through the optical fibre is based on the reflection and refraction phenomena, both being susceptible of analysis by means of the well-known Snell's laws. These laws are also applicable to every kind of optical fibre, by considering the interface between the core and the cladding to be locally plane at the reflection point [20].

2.1. Derivation of the ray path equation

The general equation for a ray path is the Eikonal equation, which may be written as follows [19–21]

$$\frac{\mathrm{d}}{\mathrm{d}s}\left(n\left(\mathbf{r}\right)\frac{\mathrm{d}\mathbf{r}}{\mathrm{d}s}\right)=\vec{\boldsymbol{\nabla}}n, \tag{1}$$

where s is the distance measured along the path, $\mathbf{r}$ is the position vector for a point on the ray path, $\mathrm{d}\mathbf{r}/\mathrm{d}s$ is the unit vector tangent to the ray path, and z is the fibre axis.

For the calculations below we will consider the most general refractive index profile in MSI fibres, which can be expressed as

$$n\left(r\right)=\begin{cases} n_1; & r<\rho_1,\\ n_2; & \rho_1\leqslant r<\rho_2,\\ \quad\vdots & \\ n_N;\ \rho_{N-1}\leqslant r<\rho_N,\\ n_{\mathrm{cl}}; & r\geqslant\rho_N. \end{cases} \tag{2}$$

For the sake of simplicity, we will neglect the possible effects of the protective jacket, assuming that the cladding extends to infinity.

2.2. Ray invariants and classification of rays

If we use cylindrical coordinates (r, ψ, z) and name the angle between the ray path and the longitudinal axis θ_{z_i}, then from the ray path equation we can derive the ray invariant $\tilde{\beta}$ as

$$\tilde{\beta}=n_i\cos\theta_{z_i}=\begin{cases} n_1\cos\theta_{z_1}; & r<\rho_1,\\ n_2\cos\theta_{z_2}; & \rho_1\leqslant r<\rho_2,\\ \quad\vdots & \\ n_N\cos\theta_{z_N};\ \rho_{N-1}\leqslant r<\rho_N,\\ n_{\mathrm{cl}}\cos\theta_t; & r\geqslant\rho_N, \end{cases} \tag{3}$$

which is related to the translational invariance of the MSI fibre.

Additional operations on the ray path equation lead to the invariant $\tilde{l}$ given by the dimensionless form

$$\tilde{l}=\frac{\rho_i}{\rho_N}n_i\sin\theta_{z_i}\cos\theta_{\phi_i};\qquad i=1\ldots N, \tag{4}$$

which accounts for the azimuthal symmetry of the fibre. θ_{ϕ_i} is the angle that the tangent to the interface between two consecutive layers makes with the path projection onto the fibre cross-section. Fig. 1 shows the angles used to define both ray invariants.

The ray invariants $\tilde{\beta}$ and $\tilde{l}$ are very important quantities because they allow us to instantly determine the direction of the ray at any position along its trajectory. They are not independent of each other, since they are related by Snell's law.

Using the definition of the ray invariants, the radial component of the ray path equation yields

$$g\left(r\right)=\tilde{\beta}^2\left(\frac{\mathrm{d}r}{\mathrm{d}z}\right)^2=n^2\left(r\right)-\tilde{\beta}^2-\frac{\tilde{l}^2\rho_N^2}{r^2}. \tag{5}$$

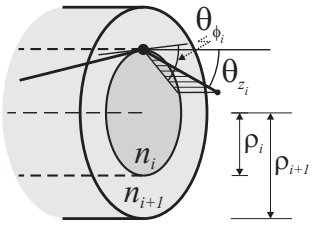

Figure 1 Definition of the angles θ_{z_i} and θ_{ϕ_i}.

© 2008 by WILEY-VCH Verlag GmbH & Co. KGaA, Weinheim

A convenient way to classify rays in MSI fibres is to make use of the ray path equation $g(r)$ to determine the range of values of the radial coordinate r for which rays can propagate [20]. Ray paths can exist only if the right-side of Eq. (5) is non-negative, corresponding to an oscillating field, whereas we have an evanescent field if the right-side of Eq. (5) is negative [20, 22–24].

Taking this into account, we can classify rays as follows:

– *Bound rays:* These rays are bound to the fibre core and do not leak into the cladding,

$$\begin{cases} n_{\mathrm{cl}} \leqslant \tilde{\beta} \leqslant n_1, \\ 0 \leqslant \tilde{l} \leqslant \tilde{l}_{\max}\left(\tilde{\beta}\right). \end{cases} \tag{6}$$

– *Tunnelling rays:* These rays lose slowly part of their power to the cladding by means of a tunnelling mechanism,

$$\begin{cases} 0 \leqslant \tilde{\beta} < n_{\mathrm{cl}}, \\ \left(n_{\mathrm{cl}}^2 - \tilde{\beta}^2\right)^{1/2} \leqslant \tilde{l} \leqslant \tilde{l}_{\max}\left(\tilde{\beta}\right). \end{cases} \tag{7}$$

– *Refracting rays:* These rays reach the cladding and attenuate very fast as they propagate,

$$\begin{cases} 0 \leqslant \tilde{\beta}^2 + \tilde{l}^2 < n_{\mathrm{cl}}^2. \end{cases} \tag{8}$$

In the statements above, $\tilde{l}_{\max}\left(\tilde{\beta}\right)$ is the maximum value of $\tilde{l}$ along the curve $g(r) = 0$, i.e.

$$\tilde{l}_{\max}^2\left(\tilde{\beta}\right) = \left(n_x^2 - \tilde{\beta}^2\right)\frac{\rho_x^2}{\rho_N^2}, \tag{9}$$

x being an integer value satisfying

$$x = \min\{\text{all possible values of } i\} \qquad i = 1 \ldots N$$

so that $\tilde{\beta} \geqslant \tilde{\beta}_{\min}$, and

$$\tilde{\beta}_{\min}^2 = \begin{cases} \max\left\{0, \dfrac{\rho_{j+1}^2 n_{j+1}^2 - \rho_i^2 n_i^2}{\rho_{j+1}^2 - \rho_i^2}\right\}; & \begin{cases} i = 1 \ldots N-1, \\ j = i \ldots N-1, \end{cases} \\ 0; & i = N. \end{cases} \tag{10}$$

2.3. Ray path parameters

From the knowledge of the ray path parameters, it is possible to obtain the analytical equations which describe the ray trajectories inside a fibre. This is due to the fact that each ray is fully characterised by the invariants $\tilde{\beta}$ and $\tilde{l}$ [20].

The ray path parameters are classified as follows:

– The *path length* is the distance between successive reflections, and it is very useful to calculate the attenuation suffered by each ray due to absorption.
– The *ray half-period* is the distance between successive reflections, but, in this case, measured along the symmetry axis, and it is very useful to describe ray trajectories.
– The *ray transit time* is defined as the time taken for a ray to propagate a distance along a waveguide, and it is the most important quantity required to describe pulse spreading. It is calculated as follows

$$t = \frac{1}{c}\int n\mathrm{d}s = \frac{1}{c\tilde{\beta}}\int_0^z n^2 \mathrm{d}z. \tag{11}$$

We can generalize Eq. (11) to the N layer expression

$$t = \begin{cases} \mathrm{A} \begin{cases} n_{i+1}^2 < \tilde{\beta}^2 + \dfrac{\tilde{l}^2\rho_N^2}{\rho_i^2} < n_i^2 \\ \rho_{i-1}^2 < \dfrac{\tilde{l}^2\rho_N^2}{n_i^2 - \tilde{\beta}^2} < \rho_i^2 \end{cases} & i = 1 \ldots N, \\ \mathrm{B} \begin{cases} n_{y+1}^2 < \tilde{\beta}^2 + \dfrac{\tilde{l}^2\rho_N^2}{\rho_y^2} < n_y^2 \\ \rho_{x-1}^2 < \dfrac{\tilde{l}^2\rho_N^2}{n_x^2 - \tilde{\beta}^2} < \rho_x^2 \end{cases} & \begin{cases} y = 2 \ldots N, \\ x = 1 \ldots y-1, \end{cases} \end{cases} \tag{12}$$

where

$$\mathrm{A} = \frac{z}{c\tilde{\beta}}n_i^2,$$

$$\mathrm{B} = \frac{z}{c\tilde{\beta}}\frac{\dfrac{n_x^2}{n_x^2 - \tilde{\beta}^2}G_x + \displaystyle\sum_{i=x+1}^{y}\frac{n_i^2}{n_i^2 - \tilde{\beta}^2}(G_i - H_i)}{\dfrac{1}{n_x^2 - \tilde{\beta}^2}G_x + \displaystyle\sum_{i=x+1}^{y}\frac{1}{n_i^2 - \tilde{\beta}^2}(G_i - H_i)},$$

$$G_i = \rho_i\sqrt{n_i^2 - \tilde{\beta}^2 - \frac{\tilde{l}^2\rho_N^2}{\rho_i^2}},$$

$$H_i = \rho_{i-1}\sqrt{n_i^2 - \tilde{\beta}^2 - \frac{\tilde{l}^2\rho_N^2}{\rho_{i-1}^2}},$$

and

$$\begin{cases} \rho_0 = 0, \\ n_{N+1} = n_{\mathrm{cl}}. \end{cases}$$

We will use Eq. (12) in order to calculate the impulse response of the fibre and its bandwidth.

2.4. Power transmission coefficients for leaky rays

Multimode MSI fibres can propagate leaky rays (i.e. refracting and tunnelling rays) in addition to bound rays, when

© 2008 by WILEY-VCH Verlag GmbH & Co. KGaA, Weinheim

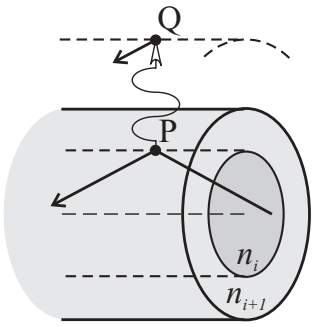

Figure 2 Trajectory of a tunnelling ray. Part of the ray power is transferred from the turning point at P to the cladding at Q.

they are illuminated by sources which emit light over a wide range of directions, as is the case of LEDs [20, 25]. These leaky rays are responsible for the loss of power by radiation and, therefore, they have a great significance in the description of light propagation within a multimode MSI fibre [26].

Compared to refracting rays, tunnelling rays undergo a very slow leakage and, therefore, they play a major role in the determination of the power attenuation along a fibre [27, 28]. Tunnelling rays disappear in the core at the turning points and reappear in the cladding at a finite distance from the core-cladding interface. For these rays to be able to propagate in the cladding, it is necessary to have a positive $g(r)$ for all values of r beyond a certain radius $r_{\rm rad}$ given by the condition $g(r)|_{r=r_{\rm rad}} = 0$. Hence

$$r_{\rm rad} = \frac{\tilde{l}\rho_N}{\left(n_{\rm cl}^2 - \tilde{\beta}^2\right)^{1/2}}. \tag{13}$$

The trajectory of a tunnelling ray is shown in Fig. 2.

At each turning point, part of the ray power is lost to the cladding by means of a tunnelling mechanism, which is analogous to the frustrated total internal reflection [29–33]. This mechanism is caused by the curvature of the core-cladding interface [27]. The ray theory does not serve to understand the physical mechanism that produces this type of radiation [34]. Its explanation has to be looked for by using Maxwell's equations and, more specifically, the modal solution of the wave equation [25, 35].

Nevertheless, we can still retain the ray paths of geometric optics and incorporate this wave effect by conveniently defining a power transmission coefficient T and assuming that power loss occurs only at turning points along the ray path [20]. Furthermore, such an approach has the additional advantage of allowing us to extend its applicability to the analysis of refracting rays. Therefore, we define T as the fraction of incident power transmitted to the cladding

$$T = 1 - \frac{\text{power of the reflected ray}}{\text{power of the incident ray}}. \tag{14}$$

The evaluation of this power transmission coefficient by an electromagnetic-mode analysis presents a boundary-value problem that is virtually intractable for geometries involving more than two layers [28], which is the usual

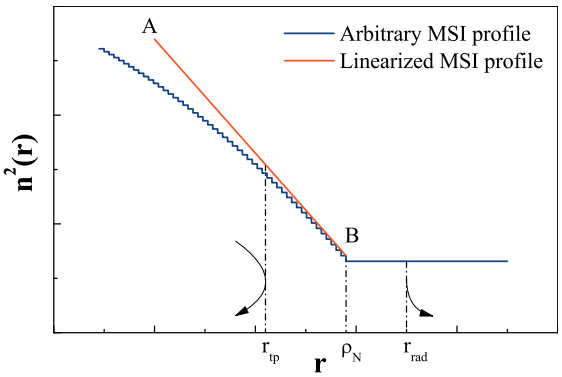

Figure 3 (online color at: www.lpr-journal.org) The linearized profile used in the analysis corresponds to $\overline{AB}$ (red line). At $r_{\rm tp}$ the ray is partially reflected and the position $r_{\rm rad}$ in the cladding stands for the point where the transmitted ray reappears.

case in MSI fibres. We can overcome such a problem if we linearize the square of the core refractive index in the profile of the MSI fibre at the top of the jump at $r = \rho_N$, as shown in Fig. 3 [28, 36]. We obtain

$$n^2(r) = \begin{cases} \delta(r - \rho_N) + n_N^2; & r \lesssim \rho_N, \\ n_{\rm cl}^2; & r \gtrsim \rho_N, \end{cases} \tag{15}$$

where n_N is the refractive index and ρ_N is the outer radius of the Nth layer (i.e. the outermost one).

The value of δ is the slope of the core profile at $r = \rho_N^-$

$$\delta = \left.\frac{{\rm d}n^2(r)}{{\rm d}r}\right|_{r=\rho_N^-} = \frac{n_N^2 - n_{N-1}^2}{\rho_N - \rho_{N-1}}, \tag{16}$$

and $\delta < 0$ whenever the refractive index profile decreases with r.

Provided that the change in the refractive index profile over this region is small, i.e. that we are considering weakly guiding fibres, the results obtained are independent of polarization [37]. By assuming that $k\rho_N \gg 1$, so that the fields exhibit local-plane-wave, or ray, characteristics [38, 39], we can work with the solutions of the scalar wave equation. ($k = 2\pi/\lambda$ is the wavenumber and λ the wavelength in vacuum.)

The linearization of $n^2(r)$ in Eq. (15) allows us to calculate these solutions by following the same procedure as for SI and GI fibres, which is accurately described in [40].

Using the ray invariants given by Eqs. (3) and (4), we determine the power transmission coefficient as [40]

$$T = \frac{4}{\pi^2}\frac{C_2}{X^2 + Y^2}, \tag{17}$$

© 2008 by WILEY-VCH Verlag GmbH & Co. KGaA, Weinheim

where the coefficients X and Y are given by

$$X = -A_1' A_2 + B_1' B_2 + A_1 \left(C_1 A_2 - C_2 A_2'\right) - B_1 \left(C_1 B_2 - C_2 B_2'\right),$$

$$Y = A_1' B_2 + B_1' A_2 - B_1 \left(C_1 A_2 - C_2 A_2'\right) - A_1 \left(C_1 B_2 - C_2 B_2'\right),$$

where

$$A_1 \equiv \mathrm{Ai}\left(\xi_1\right), \qquad B_1 \equiv \mathrm{Bi}\left(\xi_1\right),$$

$$A_2 \equiv \mathrm{Ai}\left(\xi_2\right), \qquad B_2 \equiv \mathrm{Bi}\left(\xi_2\right),$$

prime denotes differentiation with respect to the arguments, and $\mathrm{Ai}\left(\xi\right)$ and $\mathrm{Bi}\left(\xi\right)$ denote the Airy functions [41]. For the profile given in Eq. (15), ξ_1 is evaluated by performing a numerical integration

$$\xi_1 = \begin{cases} -\left[\dfrac{3}{2}\displaystyle\int_{\rho_N}^{r_{\mathrm{tp}}} k_{r_1}\left(r\right) \mathrm{d}r\right]^{2/3}; & \text{if } k_{r_1}^2 > 0, \\ +\left[\dfrac{3}{2}\displaystyle\int_{r_{\mathrm{tp}}}^{\rho_N} \left|k_{r_1}\left(r\right)\right| \mathrm{d}r\right]^{2/3}; & \text{if } k_{r_1}^2 < 0, \end{cases} \tag{18}$$

whereas ξ_2 is readily calculated as

$$\xi_2 = \begin{cases} -\left[\dfrac{3}{2} k \rho_N \left\{\left(n_{\mathrm{cl}}^2 - \tilde{\beta}^2 - \tilde{l}^2\right)^{1/2} - \tilde{l} \arccos\left[\dfrac{\tilde{l}}{\left(n_{\mathrm{cl}}^2 - \tilde{\beta}^2\right)^{1/2}}\right]\right\}\right]^{2/3}; & \text{if } k_{r_2}^2 > 0, \\ +\left[\dfrac{3}{2} k \rho_N \left\{\tilde{l} \ln\left[\dfrac{\tilde{l} + \left(\tilde{\beta}^2 + \tilde{l}^2 - n_{\mathrm{cl}}^2\right)^{1/2}}{\left(n_{\mathrm{cl}}^2 - \tilde{\beta}^2\right)^{1/2}}\right] - \left(\tilde{\beta}^2 + \tilde{l}^2 - n_{\mathrm{cl}}^2\right)^{1/2}\right\}\right]^{2/3}; & \text{if } k_{r_2}^2 < 0, \end{cases} \tag{19}$$

$k_{r_1}^2 \equiv k_{r_1}^2\left(\rho_N\right)$ and $k_{r_2}^2 \equiv k_{r_2}^2\left(\rho_N\right)$ being given by

$$k_{r_1}\left(r\right) = \begin{cases} k\left[n^2\left(r\right) - \tilde{\beta}^2 - \dfrac{\tilde{l}^2 \rho_N^2}{r^2}\right]^{1/2}; & \text{if } n^2\left(r\right) > \tilde{\beta}^2 + \dfrac{\tilde{l}^2 \rho_N^2}{r^2}, \\ \imath k\left[\tilde{\beta}^2 + \dfrac{\tilde{l}^2 \rho_N^2}{r^2} - n^2\left(r\right)\right]^{1/2}; & \text{if } n^2\left(r\right) < \tilde{\beta}^2 + \dfrac{\tilde{l}^2 \rho_N^2}{r^2}, \end{cases} \tag{20}$$

$$k_{r_2}\left(r\right) = \begin{cases} k\left(n_{\mathrm{cl}}^2 - \tilde{\beta}^2 - \dfrac{\tilde{l}^2 \rho_N^2}{r^2}\right)^{1/2}; & \text{if } n_{\mathrm{cl}}^2 > \tilde{\beta}^2 + \dfrac{\tilde{l}^2 \rho_N^2}{r^2}, \\ \imath k\left(\tilde{\beta}^2 + \dfrac{\tilde{l}^2 \rho_N^2}{r^2} - n_{\mathrm{cl}}^2\right)^{1/2}; & \text{if } n_{\mathrm{cl}}^2 < \tilde{\beta}^2 + \dfrac{\tilde{l}^2 \rho_N^2}{r^2}. \end{cases} \tag{21}$$

In Eq. (18), r_{tp} is the root of $k_{r_1}\left(r\right) = 0$ [20]

$$r_{\mathrm{tp}} = -\frac{1}{3\delta}\left[b + \frac{1}{2^{1/3}}\left(L + \sqrt{3}M\right)\right], \tag{22}$$

where

$$L = \left(F^2 + G^2\right)^{1/6} \cos\left[\frac{1}{3}\arctan\left(\frac{G}{F}\right)\right],$$

$$M = \left(F^2 + G^2\right)^{1/6} \sin\left[\frac{1}{3}\arctan\left(\frac{G}{F}\right)\right],$$

$$F = -2b^3 - 27\delta^2 c,$$

$$G = 3\sqrt{3}\left(-4\delta^2 b^3 c - 27\delta^4 c^2\right)^{1/2},$$

$$b = -\delta\rho_N + n_N^2 - \tilde{\beta}^2,$$

$$c = -\tilde{l}^2 \rho_N^2.$$

The coefficients C_1 and C_2, which also depend on another four coefficients M_1, M_2, L_1 and L_2, are shown below

$$C_1 = \left(L_2 - L_1\right)/M_1, \qquad C_2 = -M_2/M_1,$$

$$M_1 = \frac{k_{r_1}}{\left(-\xi_1\right)^{1/2}}, \qquad M_2 = \frac{-k_{r_2}}{\left(-\xi_2\right)^{1/2}},$$

$$L_1 = \frac{-k_{r_1}}{4\left(-\xi_1\right)^{3/2}} - \frac{k_{r_1}'}{2k_{r_1}}, \qquad L_2 = \frac{k_{r_2}}{4\left(-\xi_2\right)^{3/2}} - \frac{k_{r_2}'}{2k_{r_2}},$$

© 2008 by WILEY-VCH Verlag GmbH & Co. KGaA, Weinheim

where

$$k'_{r_1} = \begin{cases} k\dfrac{\tilde{l}^2/\rho_N + \delta/2}{\left(n_N^2 - \tilde{\beta}^2 - \tilde{l}^2\right)^{1/2}}; & \text{if } k_{r_1}^2 > 0, \\ \imath k\dfrac{-\tilde{l}^2/\rho_N - \delta/2}{\left(\tilde{\beta}^2 + \tilde{l}^2 - n_N^2\right)^{1/2}}; & \text{if } k_{r_1}^2 < 0, \end{cases} \tag{23}$$

$$k'_{r_2} = \begin{cases} k\dfrac{\tilde{l}^2/\rho_N}{\left(n_{\mathrm{cl}}^2 - \tilde{\beta}^2 - \tilde{l}^2\right)^{1/2}}; & \text{if } k_{r_2}^2 > 0, \\ \imath k\dfrac{-\tilde{l}^2/\rho_N}{\left(\tilde{\beta}^2 + \tilde{l}^2 - n_{\mathrm{cl}}^2\right)^{1/2}}; & \text{if } k_{r_2}^2 < 0. \end{cases} \tag{24}$$

2.5. Distribution of the power transmission coefficient in terms of the ray invariants

In order to illustrate the significance and the extension of tunnelling rays we will analyse the "Eska-Miu" MSI-POF from Mitsubishi [12] and the "TVER" MSI-POF [13]. The former has three layers, whereas the latter has four. Their refractive index profiles, measured with the aid of the inverse near-field method [42, 43], and the physical dimensions of the different layers are reproduced in Fig. 4 and in Table 1.

We have chosen characteristics typical of PMMA-based POFs: we have taken the value of 1.492 as the refractive index of the innermost layer (n_1), considering a value of 1.402 as the refractive index of the cladding (n_{cl}), yielding a peak numerical aperture of 0.51. The refractive indices of the remaining layers in between have been adjusted according to the measured refractive index profiles in Fig. 4 relative to the extreme values n_1 and n_{cl}.

The contour plots in Fig. 5 show the numerical results for the power transmission coefficient of Eq. (17) as a function of the square of the ray invariants $\tilde{\beta}$ and $\tilde{l}$ for the wavelength $\lambda = 650\,\mathrm{nm}$.

The dashed dotted line superimposed on the $\tilde{\beta}^2$-$\tilde{l}^2$ plane shows the limit where a tunnelling ray becomes a refracting one. In MSI fibres this boundary extends along the whole $\tilde{\beta}^2$-$\tilde{l}^2$ plane, or more specifically, from $(0, n_{\mathrm{cl}}^2)$ to $(n_{\mathrm{cl}}^2, 0)$.

It can be observed that the region of tunnelling rays in the TVER fibre is quite small, whereas the Eska-Miu exhibits a wider region of tunnelling rays (their proportion to bound rays is also more significant). In order to be able to understand the reason for such a behaviour, we have to refer to their refractive index profiles (see Figs. 4(a) and 4(b)). Although the outermost layer of the Eska-Miu fibre is extremely thin, the great difference between the refractive indices of this layer and the cladding allows greater values of $\tilde{l}^2_{\mathrm{max}}$ in Eq. (9) and, therefore, this leads to a much greater extension of the region of tunnelling rays than in the case of the TVER fibre, where this difference is smaller. Therefore, the significance of tunnelling rays in MSI fibres is subjected to the refractive index profile.

Tunnelling rays can propagate long distances before being completely attenuated because, in most cases, their power transmission coefficient is close to 0. This fact suggests that tunnelling rays should be taken into account in geometric optics and, therefore, it would be preferable the assignment of a simplified value of $T = 0$ to tunnelling rays to a rejection of them.

Table 1 Physical dimensions of the different layers of the investigated MSI-POFs. The outer radius of each ith layer is denoted by ρ_i and it is measured in μm.

	ρ_1	ρ_2	ρ_3	ρ_4
Eska-Miu	250	350	380	–
TVER	160	230	270	330

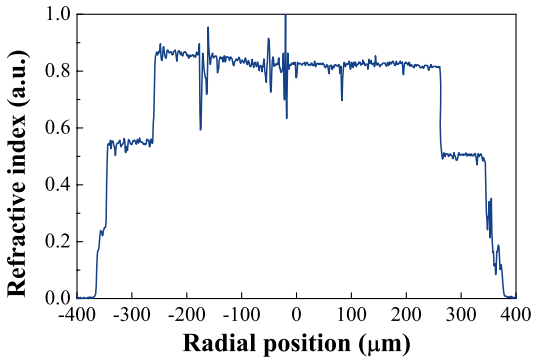

(a) Eska-Miu fibre.

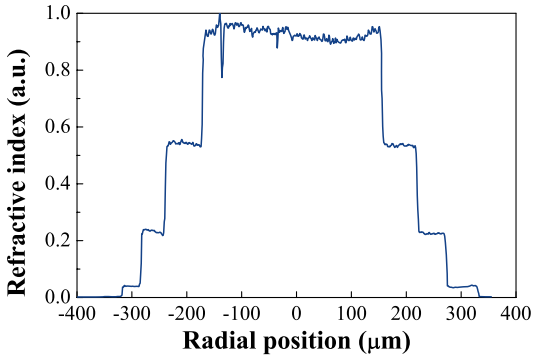

(b) TVER fibre.

Figure 4 (online color at: www.lpr-journal.org) Refractive-index profiles of the investigated MSI-POFs.

3. Analysis of coupling losses

The insertion loss of a fibre splice or a connector is the primary measure of its quality. For this reason, in the process of splicing or in the design of a connector it is of critical importance to understand and evaluate the sources of loss

© 2008 by WILEY-VCH Verlag GmbH & Co. KGaA, Weinheim

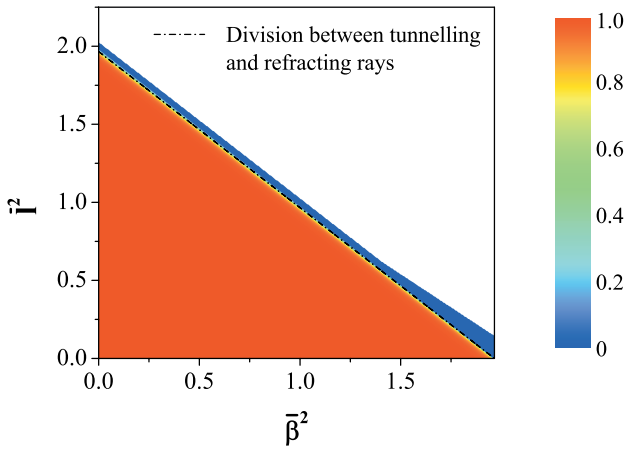

(a) Eska-Miu fibre.

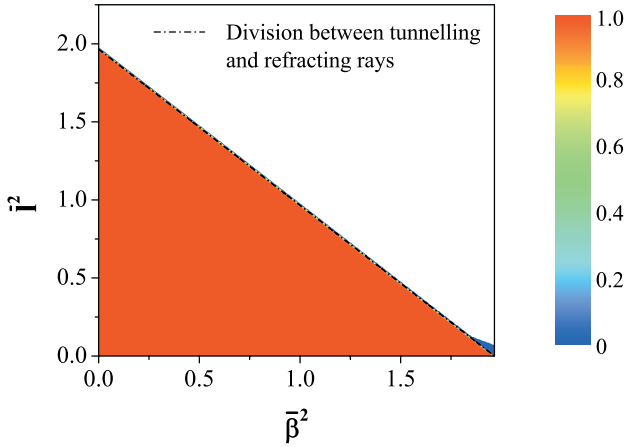

(b) TVER fibre.

Figure 5 (online color at: www.lpr-journal.org) Contour plots of the power transmission coefficient T on the $\tilde{\beta}^2$-$\tilde{l}^2$ plane, calculated for both tunnelling and refracting rays and for the wavelength $\lambda = 650$ nm. The dashed dotted line shows the limit where a tunnelling ray becomes a refracting ray.

in fibre-to-fibre coupling, which are classified as extrinsic and intrinsic coupling losses.

3.1. Extrinsic coupling loss

Mechanical misalignment is a major source of extrinsic coupling losses when joining two fibres [44, 45]. The most important types of misalignments between fibres are the longitudinal separation, the axial or transverse offset, and the angular misalignment, as shown in Fig. 6. We present below the theoretical calculations, assuming in all cases a uniform optical power density.

In the case of the longitudinal separation, we have to calculate the total power $P_{\rm ac}$ accepted by the receiving fibre when the fibre ends are longitudinally separated by a gap

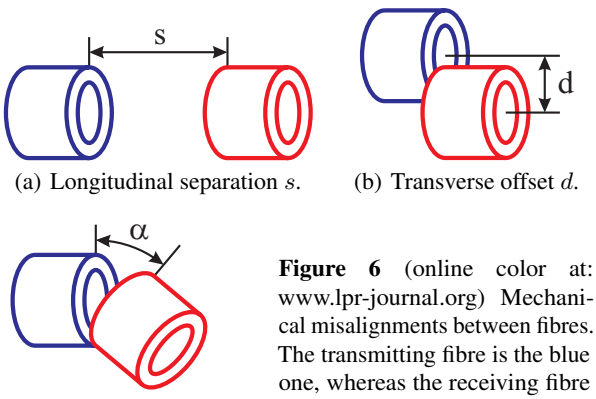

(a) Longitudinal separation s. (b) Transverse offset d.

(c) Angular misalignment α.

Figure 6 (online color at: www.lpr-journal.org) Mechanical misalignments between fibres. The transmitting fibre is the blue one, whereas the receiving fibre is the red one.

s [45–48]. We have

$$L_{LS} = -10 \log \frac{P_{\rm ac}}{P_{\rm br}}, \tag{25}$$

which is valid for $s \leqslant \rho_1 / \tan\theta_2$, with

$$P_{\rm ac} = P_1^1 + \sum_{i=2}^{p} P_1^i + \sum_{j=2}^{q} P_j^1 + \sum_{j=2}^{N} \sum_{i=u}^{v} P_j^i,$$

$$P_{\rm br} = \pi^2 \frac{I_0}{n_0^2} \sum_{i=1}^{N} \left(\rho_i^2 - \rho_{i-1}^2\right) NA_i^2,$$

where $NA_i = \left(n_i^2 - n_{\rm cl}^2\right)^{1/2}$ is the local numerical aperture, I_0 is the maximum intensity of a Lambertian light source, n_0 the refractive index of the source medium, and

$$\theta_i = \arcsin \frac{NA_i}{n_0}.$$

P_j^i denotes the power contribution of the ith layer of the transmitting fibre to the jth layer of the receiving fibre, i.e.

$$P_1^1 = \frac{\pi^2 I_0}{n_0^2} \frac{NA_1^2}{\left(\rho_1 + s\tan\theta_1\right)^2} \rho_1^4,$$

$$P_1^{i \geqslant 2} = \frac{\pi^2 I_0}{n_0^2} \frac{NA_i^2}{\left\{1 + \dfrac{2s\tan\theta_i}{\rho_i - \rho_{i-1}}\right\}} \times \left[\rho_1^2 - \left(\rho_{i-1} - s\tan\theta_i\right)^2\right],$$

$$P_{j \geqslant 2}^1 = \frac{\pi^2 I_0}{n_0^2} \frac{\rho_1^2 NA_j^2}{\left(\rho_1 + s\tan\theta_1\right)^2} \times \left[\min\left\{\rho_j^2, \left(\rho_1 + s\tan\theta_1\right)^2\right\} - \rho_{j-1}^2\right],$$

© 2008 by WILEY-VCH Verlag GmbH & Co. KGaA, Weinheim

$$P_{j\geqslant 2}^{i\geqslant 2}=\begin{cases}\dfrac{\pi^2 I_0}{n_0^2}\dfrac{NA_j^2}{\left\{1+\dfrac{2s\tan\theta_i}{\rho_i-\rho_{i-1}}\right\}} \\ \times\left[\min\left\{\rho_j^2,(\rho_i+s\tan\theta_i)^2\right\}\right. \\ \left.-\max\left\{\rho_{j-1}^2,(\rho_{i-1}-s\tan\theta_i)^2\right\}\right]; \\ \qquad\qquad\qquad\qquad \text{if } i<j, \\ \dfrac{\pi^2 I_0}{n_0^2}\dfrac{NA_i^2}{\left\{1+\dfrac{2s\tan\theta_i}{\rho_i-\rho_{i-1}}\right\}} \\ \times\left[\min\left\{\rho_j^2,(\rho_i+s\tan\theta_i)^2\right\}\right. \\ \left.-\max\left\{\rho_{j-1}^2,(\rho_{i-1}-s\tan\theta_i)^2\right\}\right]; \\ \qquad\qquad\qquad\qquad \text{if } i\geqslant j.\end{cases}$$

The integers p, q, u and v are the limits of integration, satisfying

$$p=\max\{\text{all possible values of } k\} \text{ so that}$$
$$\rho_{k-1}-s\tan\theta_k<\rho_1;\quad p=2\ldots N,$$
$$q=\max\{\text{all possible values of } k\} \text{ so that}$$
$$\rho_{k-1}\leqslant\rho_1+s\tan\theta_1<\rho_k;\quad q=2\ldots N,$$
$$u=\min\{\text{all possible values of } k\} \text{ so that}$$
$$(\rho_k+s\tan\theta_k\geqslant\rho_{j-1}) \text{ and } (\rho_{k-1}-s\tan\theta_k<\rho_j);$$
$$2\leqslant u\leqslant v\leqslant N,$$
$$v=\max\{\text{all possible values of } k\} \text{ so that}$$
$$(\rho_k+s\tan\theta_k\geqslant\rho_{j-1}) \text{ and } (\rho_{k-1}-s\tan\theta_k<\rho_j);$$
$$2\leqslant u\leqslant v\leqslant N.$$

In the case of the transverse offset, denoted by d, the power coupled into the receiving fibre is calculated by integrating the power density over the overlap region between the transmitting and receiving fibres [47, 49]. Thus we obtain

$$L_{TO}=-10\log\left(2\left[\pi\sum_{i=1}^{N}\left(\rho_i^2-\rho_{i-1}^2\right)NA_i^2\right]^{-1}\right.$$
$$\times\left\{\sum_{i=j+1}^{N}NA_i^2A_i+NA_j^2\right. \tag{26}$$
$$\left.\left.\times\left[\rho_j^2\arccos\frac{d}{2\rho_j}-\frac{d}{2}\left(\rho_j^2-d^2/4\right)^{1/2}\right]\right\}\right),$$

where

$$A_i=\rho_i^2\arccos\frac{d}{2\rho_i}-\rho_{i-1}^2\arccos\frac{d}{2\rho_{i-1}}$$
$$+\frac{d}{2}\left\{\left(\rho_{i-1}^2-d^2/4\right)^{1/2}-\left(\rho_i^2-d^2/4\right)^{1/2}\right\},$$

and j is an integer value that satisfies

$$\rho_{j-1}\leqslant d/2<\rho_j.$$

Finally, in the case of the angular misalignment, quantifying the incurred losses in MSI fibres may involve cumbersome calculations. Nevertheless, we can obtain a simple and relatively accurate expression for an angular misalignment α, provided that it is sufficiently small ($\alpha\leqslant 10°$), if the following assumptions are made [24, 44]:

- the amount of power lost outside the area of the receiving fibre is neglected, and
- the losses due solely to the angular misalignment are obtained without taking into account the refraction effect.

The coupling loss for the angular misalignment L_{AM} is

$$L_{AM}=-10\log\left(2\left[\pi\sum_{i=1}^{N}\left(\rho_i^2-\rho_{i-1}^2\right)NA_i^2\right]^{-1}\right.$$
$$\times\left\{\sum_{i=2}^{j}NA_i^2\delta_i+NA_1^2\rho_1^2\right.$$
$$\left.\left.\times\left[\arccos q_1-q_1\left(1-q_1^2\right)^{1/2}\right]\right\}\right), \tag{27}$$

where

$$\delta_i=\rho_i^2\arccos q_i-\rho_{i-1}^2\arccos q_{i-1}$$
$$+\rho_{i-1}^2q_{i-1}\left(1-q_{i-1}^2\right)^{1/2}-\rho_i^2q_i\left(1-q_i^2\right)^{1/2},$$

q_i stands for

$$q_i=\frac{n_i\sin\alpha}{2\left(n_i^2-n_{\text{cl}}^2\right)^{1/2}},$$

and j is an integer value that satisfies

$$\frac{NA_{j-1}}{n_{j-1}}\leqslant\frac{\sin\alpha}{\sqrt{2}}<\frac{NA_j}{n_j}.$$

We have performed several computer simulations using the ray-tracing method in order to compare the coupling loss obtained for each mechanical misalignment and determine the most critical one. We have used a hypothetical source covering the whole input surface of the transmitting fibre and emitting a uniform mode distribution (UMD) with a numerical aperture $NA_{\text{input}}=0.65$ (ensuring that the launched rays will fill the effective solid acceptance angle of the transmitting fibre). We have launched approximately 200 000 rays into the Eska-Miu and the TVER fibres. This number ranges between an upper boundary delimited by the total number of modes that can propagate within the fibres and a lower boundary to ensure sufficiently smooth and accurate results. We also include the analytical results obtained from the theoretical expressions.

It is worthy of remark that our numerical simulations involve only ideal fibres, whereas in real fibres there are

© 2008 by WILEY-VCH Verlag GmbH & Co. KGaA, Weinheim

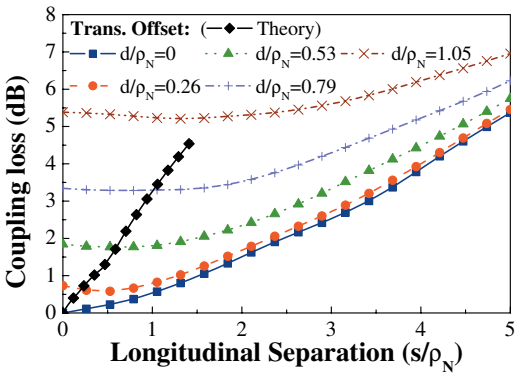

(a) Eska-Miu fibre.

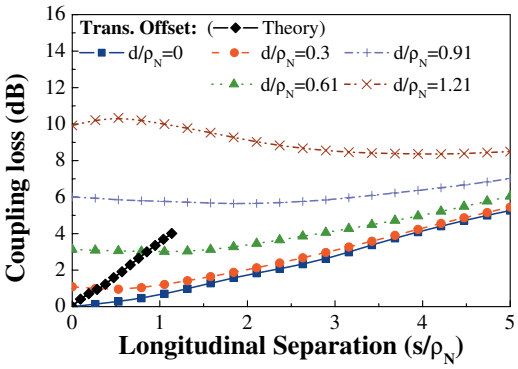

(b) TVER fibre.

Figure 7 (online color at: www.lpr-journal.org) Coupling loss against normalized longitudinal separation s/ρ_N for various transverse offsets. The analytical results are denoted by ◆.

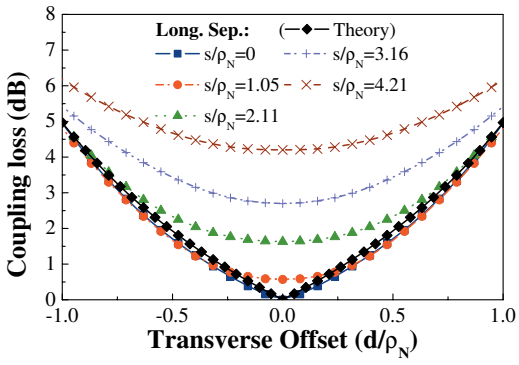

(a) Eska-Miu fibre.

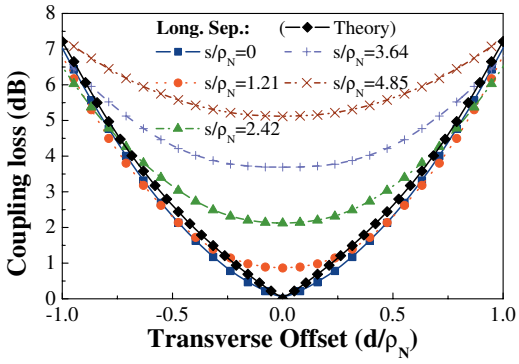

(b) TVER fibre.

Figure 8 Coupling loss against normalized transverse offset d/ρ_N for various longitudinal separations. The analytical results are denoted by ◆.

many intrinsic physical phenomena, such as differential mode attenuation and mode coupling, which can give rise to many different effects that can have an influence on the fibre transmission characteristics [50–55]. The implications of these effects are explained in detail in [16].

We have plotted on Fig. 7 the results for the coupling losses (in dB units) against the normalized longitudinal separation s/ρ_N corresponding to different transverse offsets and for both MSI-POFs (ρ_N denotes the radius of the outermost layer of the fibre, 380 μm for the Eska-Miu fibre or 330 μm for the TVER one). The analytical results superimposed on the graph are obtained using Eq. (25). Notice that the validity of this analytical formula is limited to the region where $s \leqslant \rho_1/\tan\theta_2$, which has a value of $s/\rho_N = 1.4389$ for the Eska-Miu fibre and of $s/\rho_N = 1.1595$ for the TVER fibre.

At first sight, it can be seen that the analytical expressions show fairly pessimistic values for both fibres, in contrast to the numerical results in the absence of any transverse offset ($d/\rho_N = 0$), so we can conclude that the former provide an upper bound for coupling losses.

Additionally, Fig. 7 reveals that coupling losses are more sensitive to a transverse offset than to a longitudinal separation. For instance, in the case of the Eska-Miu fibre, for a transverse offset $d/\rho_N = 1.05$ and no longitudinal separation ($s/\rho_N = 0$) coupling losses are approximately 5.4 dB, in comparison with the much lower value of 0.57 dB achieved for a longitudinal separation $s/\rho_N = 1.05$ and no transverse offset ($d/\rho_N = 0$). Therefore, low coupling losses require a very small transverse offset, whose effects will be analyzed in more detail shortly.

Let us now compare the numerical results for the Eska-Miu and TVER fibres. We can observe that, on the one hand, in the absence of any transverse offset, coupling losses are slightly higher for the Eska-Miu fibre than for the TVER fibre as longitudinal separation increases. On the other hand, coupling losses are much higher for the TVER fibre than for the Eska-Miu fibre when there is a transverse offset. Both effects rely on the fact that the distribution of light power within the layers of the fibre depends on its refractive index profile (further information can be found in [16]).

We present now in Fig. 8 the results for coupling losses as a function of the normalized offset d/ρ_N for different longitudinal separations.

By comparing the numerical results in the absence of any longitudinal separation between fibre ends ($s/\rho_N = 0$) with the analytical coupling loss, we can observe that

© 2008 by WILEY-VCH Verlag GmbH & Co. KGaA, Weinheim

the latter shows slightly higher values, since it involves overfilled mode distribution conditions. Even so, it is clear that both results are in good agreement.

Let us now compare the numerical results obtained for both MSI-POFs. In the case of the Eska-Miu fibre, a transverse offset equal to the radius of the fibre ($d/\rho_N = 1$) when there is no longitudinal separation ($s/\rho_N = 0$) leads to a coupling loss of approximately 5.0 dB. This effect is even more dramatic on the TVER fibre, whose coupling loss turns out to be 7.0 dB. Indeed, these values are certainly higher than those obtained for longitudinal separations alone (even small offsets result in high coupling losses), which is indicative of the greater importance of transverse offsets as regards coupling loss.

It can be observed that, as the longitudinal separation between fibres increases, coupling loss increases more and more slowly with the normalized transverse offset. This behaviour can be explained on the assumption that the light exiting the transmitting fibre generates a divergent cone of radiation that overlaps the cross-section of the receiving fibre. As this cone is moved along the transverse direction, the power captured inside decreases. The decrease in power is much slower when considering larger longitudinal separations, for which the cross-section of the cone of radiation is bigger, and therefore, the power distribution is smoother.

All in all the transverse offset has so far proved to be the most critical parameter when dealing with coupling losses for MSI-POFs.

Finally, the results in Fig. 9 show the behaviour of coupling loss with an angular misalignment α for different transverse offsets. In these measurements the 0-dB reference point is fixed at $d/\rho_N = 0$, $s/\rho_N = 1$, and $\alpha = 0°$.

Again, it is clear that the analytical predictions can be regarded as an upper bound for both fibres, provided that the effects of a transverse offset or a longitudinal separation are discarded.

We can observe that coupling losses depend weakly on the angular misalignment (in contrast with the high sensitivity to the transverse offset of coupling losses). Thus, it can be concluded that angular misalignments are not as critical as transverse offsets, provided that they are kept sufficiently small. In this respect, we have found that losses always remain well below 3 dB for practical values of the angular misalignment.

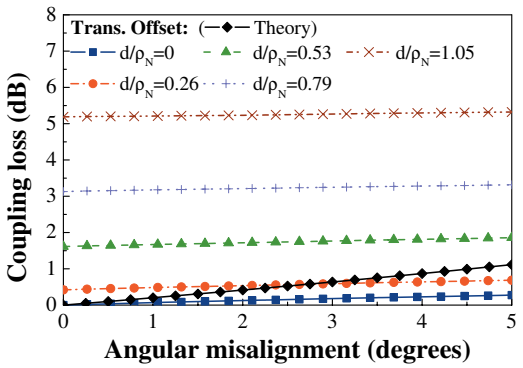

(a) Eska-Miu fibre.

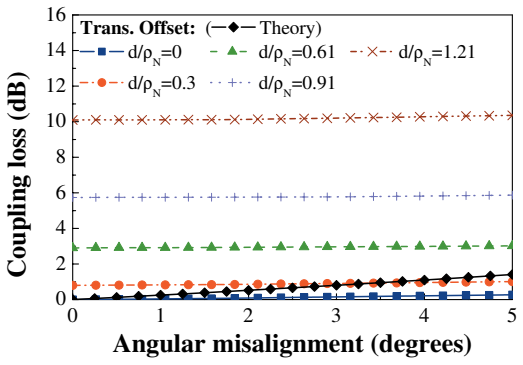

(b) TVER fibre.

Figure 9 (online color at: www.lpr-journal.org) Coupling loss against angular misalignment α (in degrees) for various transverse offsets. The analytical results are denoted by ◆.

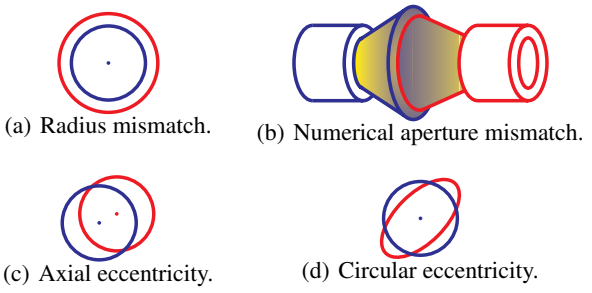

(a) Radius mismatch. (b) Numerical aperture mismatch.

(c) Axial eccentricity. (d) Circular eccentricity.

Figure 10 (online color at: www.lpr-journal.org) Variations in waveguide properties that contribute to intrinsic coupling losses. The transmitting fibre is the blue one, whereas the receiving fibre is the red one. The dots show the symmetry axes corresponding to each fibre.

3.2. Intrinsic coupling loss

The extrinsic coupling losses analysed in the previous subsection can be controlled and cancelled or, at least, minimized to a practically negligible value by improving the fibre joining techniques. Despite this fact, all methods continue to have intrinsic contributions to loss. The intrinsic coupling losses arise from the inevitable variations in waveguide properties as a result of standard manufacturing processes, which affect the light propagation characteristics of the fibres being joined. For this reason, we have investigated the effects of tolerances to each waveguide parameter, namely, the surface diameter of each core, the axial eccentricity between each core and cladding (i.e. the deviation of the concentricity between them), their circular eccentricity (or ellipticity), and the numerical aperture. This is summarized in Fig. 10.

The study of MSI fibres is complicated by the fact that they consist of several layers, which means that the

© 2008 by WILEY-VCH Verlag GmbH & Co. KGaA, Weinheim

number of parameters that are liable to vary multiply as the number of layers increases. Thus, the evaluation of intrinsic coupling losses for MSI fibres can only be tackled from a statistical point of view. Using the ray-tracing method, we have run a set of computer simulations of 5000 trials (which has proved to be enough) that involve joining two fibres randomly chosen from a given population following a normal distribution [17, 56].

Fig. 11 shows the results obtained for the coupling loss when only one of the possible waveguide parameters is varied and also when the mismatches are applied all together for the Eska-Miu and TVER MSI-POFs. The ordinate shows the cumulative percentage of fibre joints that have intrinsic coupling losses lower than the value given in the abscissa. Each waveguide parameter has a normalized standard deviation of 5%, or a value of 0.268 in the case of the circular eccentricity mismatch. It must be taken into account that the values for the circular eccentricity must be, by definition, in the interval $[0, 1)$ (since $e = (1-b^2/a^2)^{1/2}$, a being the fibre major semi-axis and b the fibre minor semi-axis). If we had chosen the value 0.5 as the normalized standard deviation of the circular eccentricity mismatch, it would be expected that approximately 227 samples would exceed the maximum allowed value out of a set of computer simulations of 5000 trials (the probability of obtaining a random deviation outside the allowed interval, i.e. outside two standard deviations, would be of 4.55%). In such cases the trial would be aborted and the value outside the scope would be replaced with a new random choice (that is, there would be a truncation of the normal distribution). In order to prevent this, a normalized standard deviation of 0.268 has been chosen, since this value assures that none of the samples of the 5000 trials will exceed the maximum value of 1.

The details of the 50% loss or median loss L_{50} and the 90% loss L_{90} are shown in Table 2. The 50% loss L_{50} denotes that 50% of the samples considered in a large statistical population of fibres following a normal distribution will have intrinsic coupling losses below such a loss value (L_{50}). The same applies to the 90% loss L_{90}.

The procedure for the random building of the receiving fibre on each trial is as follows: firstly, the innermost layer of the receiving fibre is built in accordance with a certain radius, circularity deviation and axial eccentricity, all of them following a normal random distribution, taking as the mean values those corresponding to the innermost layer of the transmitting fibre. As for the angle that describes the orientation of the innermost layer, that is to say, the angle between the major semi-axis of the layer and the reference offset direction [57], this is randomly chosen from a uniform distribution. Its numerical aperture is also randomly chosen from a normal distribution, independently of the rest of the parameters. In all cases, when a negative parameter value has been mathematically generated, the trial is aborted and a new receiving fibre is built using new random choices.

Afterwards, the next layers surrounding the innermost ones are sequentially generated randomly in a similar way,

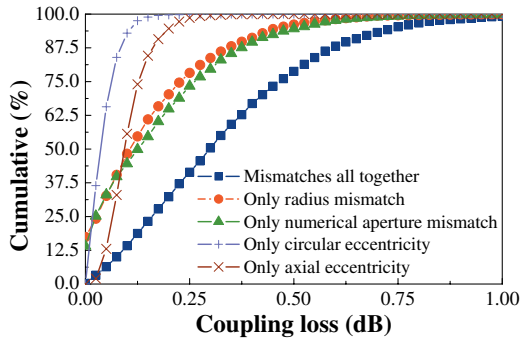

(a) Eska-Miu fibre.

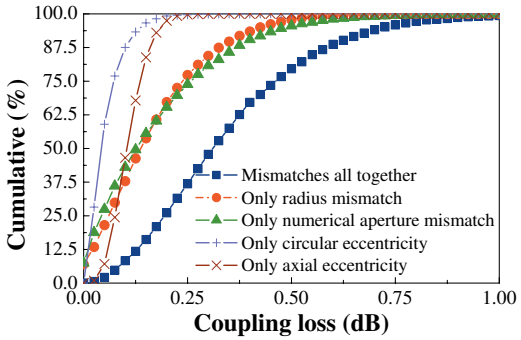

(b) TVER fibre.

Figure 11 (online color at: www.lpr-journal.org) Cumulative percentage of fibre joints having intrinsic coupling losses below a given value. Results obtained for simulations of 5000 trials by using the ray-tracing method.

the mean values now corresponding to their respective layers of the transmitting fibre. The angles that describe the orientation of each layer of the receiving fibre are randomly chosen from a uniform distribution. The same applies to the polar angles related to the transverse offset direction between the corresponding layer axes. Special care must be taken so that only positive parameter values will be accepted, avoiding overlapping of layers in which an inner layer radius results to be larger than that of a surrounding one and assuring that the numerical aperture continually decreases towards the exterior. Otherwise, the trial is aborted and a new receiving fibre is built from the beginning using new random choices. Although the use of normally distributed random deviations would in principle make it possible for absurd parameters to be mathematically generated, the previous condition prevents this kind of situations from happening.

We can observe in Fig. 11 that, when considering all the mismatches taking place simultaneously, the coupling loss is indeed the highest one. Let us now consider each of the mismatches separately. As can be seen in Fig. 11 (as well as in the statistical results gathered in Table 2), the numerical aperture and the core diameter are the most critical parameters, whereas the axial eccentricity of each core and cladding and their circular eccentricity are the least critical ones.

© 2008 by WILEY-VCH Verlag GmbH & Co. KGaA, Weinheim

	Eska-Miu fibre		TVER fibre	
	L_{50}	L_{90}	L_{50}	L_{90}
Mismatches all together	0.297	0.63	0.31	0.622
Only radius mismatch	0.106	0.379	0.135	0.353
Only numerical aperture mismatch	0.125	0.405	0.127	0.395
Only circular eccentricity	0.034	0.09	0.041	0.109
Only axial eccentricity	0.093	0.171	0.103	0.165

Table 2 Statistical results obtained for the 50% loss L_{50} and the 90% loss L_{90} measured in dB for the Eska-Miu and TVER fibres by using the ray-tracing method.

Using the information above, we have derived a compact analytical expression that allows us to evaluate intrinsic coupling losses in MSI fibres in terms of the most influential parameters. Our starting point is the total mode volume, which is a measure of the amount of launched power carried by bound rays [20]. Let us characterize the transmitting and receiving fibres by different profiles ($\rho_{1,t}$, $\rho_{2,t}$, …, $\rho_{N,t}$, $NA_{1,t}$, $NA_{2,t}$, …, $NA_{N,t}$) and ($\rho_{1,r}$, $\rho_{2,r}$, …, $\rho_{N,r}$, $NA_{1,r}$, $NA_{2,r}$, …, $NA_{N,r}$), respectively. If we consider a Lambertian light source, the total mode volume of the transmitting fibre, V_t, can be expressed as [58]

$$V_t = 2\pi^2 \sum_{i=1}^{N} \frac{\rho_{i,t}^2 - \rho_{i-1,t}^2}{2} NA_{i,t}^2. \quad (\rho_{0,t} = 0.) \tag{28}$$

The magnitude of the insertion loss when considering tolerances to each core surface diameter and each numerical aperture can be analytically evaluated, if the following assumptions are made:

- power is uniformly distributed over all modes,
- the transmitting and receiving fibres have the same number of layers N, and
- the radii of each layer for both transmitting and receiving fibres satisfy

$$\begin{cases} 0 \leqslant \rho_{1,r} \leqslant \rho_{2,t}; & i = 1, \\ \rho_{i-1,t} \leqslant \rho_{i,r} \leqslant \rho_{i+1,t}; & i = 2 \ldots N-1, \\ \rho_{N-1,t} \leqslant \rho_{N,r}; & i = N. \end{cases}$$

With these requirements, the common mode volume V_{rt}, expressed as the fraction of the mode volume of the transmitting fibre transferred to the receiving fibre, can be calculated as following [18]

$$\begin{aligned} V_{\mathrm{rt}} = 2\pi^2 \sum_{i=1}^{N} \Bigg(& \min\left\{NA_{i-1,p}^2, NA_{i,q}^2\right\} \\ & \times \frac{\max\left\{\rho_{i-1,r}^2, \rho_{i-1,t}^2\right\} - \min\left\{\rho_{i-1,r}^2, \rho_{i-1,t}^2\right\}}{2} \\ & + \min\left\{NA_{i,r}^2, NA_{i,t}^2\right\} \\ & \times \frac{\min\left\{\rho_{i,r}^2, \rho_{i,t}^2\right\} - \max\left\{\rho_{i-1,r}^2, \rho_{i-1,t}^2\right\}}{2} \Bigg), \end{aligned} \tag{29}$$

where $\rho_{0,r} = 0$, $\rho_{0,t} = 0$, $NA_{0,r} = 0$, $NA_{0,t} = 0$, and the following cases must be considered

$$\text{if } \rho_{i-1,t} \geqslant \rho_{i-1,r} \begin{cases} p = t \\ q = r \end{cases} \text{ so that } \begin{cases} NA_{i-1,p}^2 = NA_{i-1,t}^2, \\ NA_{i,q}^2 = NA_{i,r}^2, \end{cases}$$

$$\text{if } \rho_{i-1,t} < \rho_{i-1,r} \begin{cases} p = r \\ q = t \end{cases} \text{ so that } \begin{cases} NA_{i-1,p}^2 = NA_{i-1,r}^2, \\ NA_{i,q}^2 = NA_{i,t}^2. \end{cases}$$

Finally, by substituting V_{rt} for Eq. (29) and V_t for Eq. (28), the coupling loss L_{MSI} is calculated as

$$L_{MSI} = -10 \log \frac{V_{\mathrm{rt}}}{V_t}. \tag{30}$$

The third constraint in the assumptions above can be relaxed, but only at the expense of losing simplicity, since it would not be possible to obtain a compact analytical expression to calculate the intrinsic coupling loss any longer. Nevertheless, this issue can be overcome by implementing an algorithm that allows computation of V_{rt} without any restriction on the radii of each layer for both transmitting and receiving MSI fibres. The details concerning this computer algorithm are given in [18].

In order to establish the validity of the expressions obtained before, several computer simulations have been carried out. These consist in evaluating the intrinsic coupling losses when only one of the possible structural parameters is varied (namely, the numerical aperture or the core diameter) and also when the mismatches are applied all together. Each parameter has a normalized standard deviation of 5% and it is assumed to follow a normal distribution. We can adopt two different approaches to the statistical evaluation of intrinsic coupling losses:

- Applying the same normalized deviation to each waveguide parameter on every layer (the intrinsic coupling loss is obtained by means of Eq. (30) with V_{rt} calculated using Eq. (29)).
- Applying a different normalized deviation to each waveguide parameter on each layer (the intrinsic coupling loss is evaluated from Eq. (30) with V_{rt} calculated from the computer algorithm of [18]).

We believe that the latter situation describes better than the former approach the effects of mismatches that in fact may occur during manufacturing processes.

It is important to keep in mind that a uniform distribution of energy over all modes constitutes the worst case.

© 2008 by WILEY-VCH Verlag GmbH & Co. KGaA, Weinheim

Table 3 Eska-Miu fibre. Statistical results obtained for the 50% loss L_{50} and the 90% loss L_{90} measured in dB by using the analytical expressions and the ray-tracing method.

Results obtained using the same normalized deviations on every layer	**Analytical**		**Ray-tracing**	
	L_{50}	L_{90}	L_{50}	L_{90}
Mismatches all together	0.248	0.862	0.235	0.837
Only radius mismatch	0.0	0.575	0.003	0.562
Only numerical aperture mismatch	0.003	0.579	0.0	0.536

Results obtained using different normalized deviations on each layer	**Analytical**		**Ray-tracing**	
	L_{50}	L_{90}	L_{50}	L_{90}
Mismatches all together	0.276	0.64	0.263	0.617
Only radius mismatch	0.109	0.382	0.107	0.373
Only numerical aperture mismatch	0.125	0.423	0.114	0.401

Table 4 TVER fibre. Statistical results obtained for the 50% loss L_{50} and the 90% loss L_{90} measured in dB by using the analytical expressions and the ray-tracing method.

Results obtained using the same normalized deviations on every layer	**Analytical**		**Ray-tracing**	
	L_{50}	L_{90}	L_{50}	L_{90}
Mismatches all together	0.244	0.871	0.243	0.849
Only radius mismatch	0.0	0.577	0.001	0.559
Only numerical aperture mismatch	0.0	0.576	0.0	0.559

Results obtained using different normalized deviations on each layer	**Analytical**		**Ray-tracing**	
	L_{50}	L_{90}	L_{50}	L_{90}
Mismatches all together	0.302	0.624	0.295	0.608
Only radius mismatch	0.146	0.357	0.141	0.347
Only numerical aperture mismatch	0.13	0.406	0.127	0.398

Therefore, it is expected that coupling losses obtained under more realistic conditions (such as in the case of having restricted launching conditions or when including the modifications induced in the light power distribution by mode mixing) will never be higher than the limit values given by the analytical expressions.

In order to check whether the results obtained from the analytical expressions and from the ray-tracing method are comparable or not, we have plotted on Figs. 12 and 13 the results obtained for the intrinsic coupling loss when only one of the parameters is varied and also when the mismatches are applied all together, both for the Eska-Miu and the TVER MSI-POFs. The details of the 50% loss L_{50}, or median loss, and the 90% loss L_{90} for each type of fibre are shown in Tables 3 and 4.

It can be observed that the results obtained using the analytical expressions are in excellent agreement with those obtained using the ray-tracing method save the obvious minimal statistical fluctuations (the slight variations in the results are solely due to the statistical nature of the set of measurements carried out in the computer simulations). Furthermore, this coincidence happens for both MSI-POFs regardless of whether we use or not the same normalized deviation for each waveguide parameter on every layer.

Let us now compare the results obtained for the two approaches considered. Tables 3 and 4 show that the 90% loss L_{90} obtained when using different normalized deviations on each layer is certainly lower than the 90% loss obtained for the same normalized deviations on every layer, whereas the behaviour of the 50% loss L_{50} is just the opposite. This effect is especially noticeable if we consider the mismatches all together.

In order to understand the reason for having such a behaviour, we have to analyse how the random deviations are applied in each of the approaches. In both cases, we have the same probabilities of coming across a positive or negative random deviation. A negative one (meaning that the receiving fibre has a lower numerical aperture or a smaller core diameter) produces some loss, whereas a positive one leads to no loss at all.

If we consider the approach in which the same normalized deviation is applied to each waveguide parameter on every layer, a negative normalized deviation always affects negatively the rest of the layers. In contrast, in the case of the approach in which a different normalized deviation is applied to each waveguide parameter on each layer, the fact that a negative deviation has occurred on a certain layer does not imply that the same will happen on the rest of the layers. For this reason, it is expected that the 90% loss L_{90} obtained for the latter approach will be more optimistic than that for the former one.

A similar reasoning applies to the median loss L_{50}, since a positive random deviation (its probability being the same as that of a negative one) obtained for a certain waveguide parameter will have a more positive effect (for the population of fibre joints having losses below L_{50}) when the deviation is applied to every layer of the fibre, and a more negative effect when entirely different random deviations are applied.

4. Bandwidth analysis

In this section we present a numerical analysis of the pulse dispersion and bandwidth in MSI fibres under different light source configurations. For this purpose, the computational model we have developed assumes that mode coupling is absent and neglects the effects of material dispersion, which

© 2008 by WILEY-VCH Verlag GmbH & Co. KGaA, Weinheim

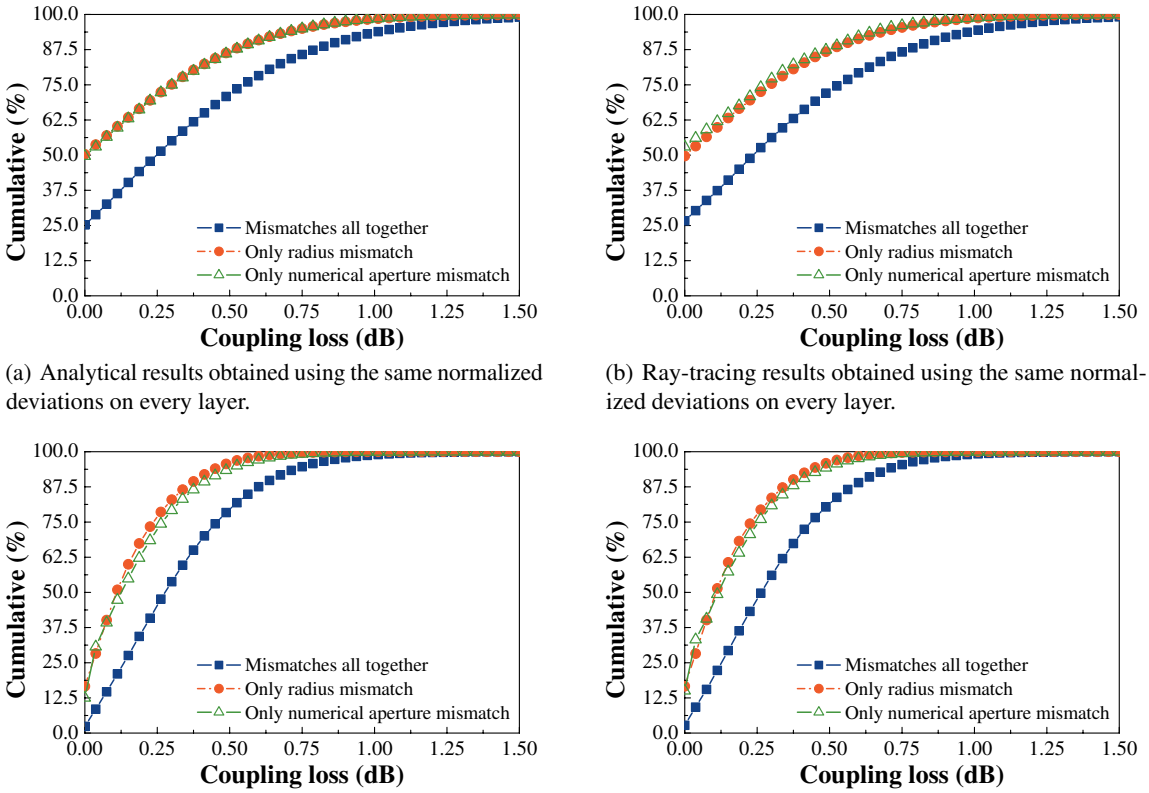

(a) Analytical results obtained using the same normalized deviations on every layer.

(b) Ray-tracing results obtained using the same normalized deviations on every layer.

(c) Analytical results obtained using different normalized deviations on each layer.

(d) Ray-tracing results obtained using different normalized deviations on each layer.

Figure 12 (online color at: www.lpr-journal.org) Eska-Miu fibre. Cumulative percentage of fibre joints having intrinsic coupling losses below a given value.

is overridden by intermodal dispersion due to the high numerical aperture of these fibres. Additionally, we study the influence of tunnelling rays on pulse propagation, which in some cases can be strong enough to cause a significant decrease in fibre bandwidth.

4.1. Description of the computational model

Our computational model relies on the calculation of the ray trajectories inside an MSI fibre by using the ray invariants $\tilde{\beta}$ and $\tilde{l}$ defined in Eqs. (3) and (4), respectively. From the knowledge of the ray transit time $t(\tilde{\beta}, \tilde{l})$ given by Eq. (12), the computational model is able to calculate the time distribution of power at any distance z along the fibre for any launching condition, i.e. the fibre impulse response $Q(t)$ [20, 59–62].

Following a similar procedure as that stated in [59], the power launched by a certain source at the input surface of the fibre is properly mapped onto the $\tilde{\beta}$-$\tilde{l}$ plane, that is to say we assign each of the launched rays the proper value $(\tilde{\beta}_{\rm ray}, \tilde{l}_{\rm ray})$ with power $\Delta P_{\rm ray}$ according to the distribution of the excited power density in the $\tilde{\beta}$-$\tilde{l}$ plane. By calculating the transit time $t(\tilde{\beta}_{\rm ray}, \tilde{l}_{\rm ray})$ for each ray, and by dividing the interval of ray arrival times into N_T time slots, the model constructs a discretized version of the impulse response $Q_i \equiv Q(t_i)$ by assigning $\Delta P_{\rm ray}$ (i.e. $Q_i = Q_i + \Delta P_{\rm ray}$) to the ith time slot given by

$$t_i \leqslant t(\tilde{\beta}_{\rm ray}, \tilde{l}_{\rm ray}) \leqslant t_{i+1}. \tag{31}$$

Let us define R_m as the mth moment of the impulse response [20, 63, 64]

$$\begin{aligned} R_m &= \int_{t_{\min}}^{t_{\max}} t^m Q(t) \mathrm{d}t \\ &= \left(\frac{1}{2} t_1^m Q_1 + \sum_{i=2}^{N_T - 1} t_i^m Q_i + \frac{1}{2} t_{N_T}^m Q_{N_T} \right) \frac{t_{N_T} - t_1}{N_T}, \end{aligned} \tag{32}$$

where $t_{N_T} \equiv t_{\max}$ and $t_1 \equiv t_{\min}$ are the transit times corresponding to the slowest and fastest propagating rays, respectively, and we use the extended trapezoidal rule to perform the integration above [41, 65].

© 2008 by WILEY-VCH Verlag GmbH & Co. KGaA, Weinheim

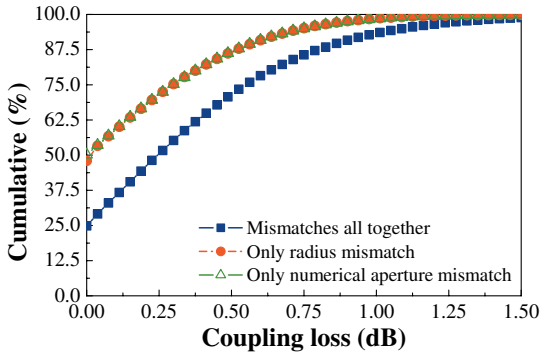

(a) Analytical results obtained using the same normalized deviations on every layer.

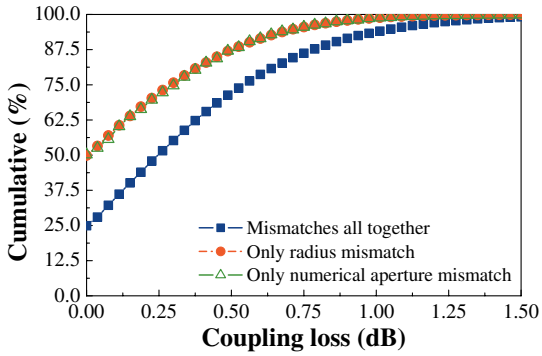

(b) Ray-tracing results obtained using the same normalized deviations on every layer.

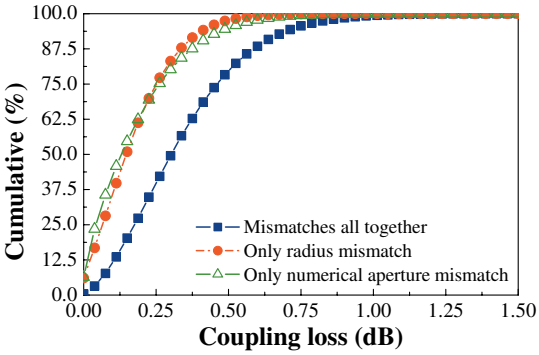

(c) Analytical results obtained using different normalized deviations on each layer.

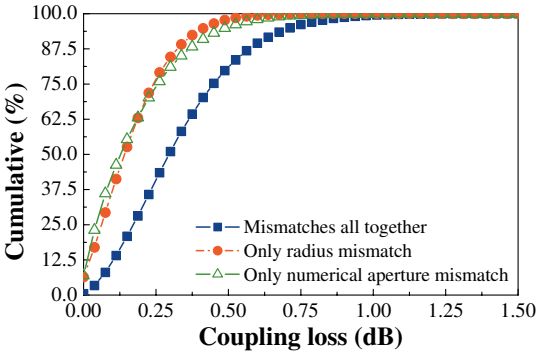

(d) Ray-tracing results obtained using different normalized deviations on each layer.

Figure 13 (online color at: www.lpr-journal.org) TVER fibre. Cumulative percentage of fibre joints having intrinsic coupling losses below a given value.

The mean transit time of the impulse response is then calculated by

$$\bar{t} = \frac{\int_{t_{\min}}^{t_{\max}} tQ(t)\mathrm{d}t}{\int_{t_{\min}}^{t_{\max}} Q(t)\mathrm{d}t} = \frac{R_1}{R_0}, \tag{33}$$

and the root-mean-square (rms) pulse width, which contains information about the power distribution and the width of the pulse [63, 66], is given by

$$\sigma = \left[\frac{\int_{t_{\min}}^{t_{\max}} (t-\bar{t})^2\, Q(t)\mathrm{d}t}{\int_{t_{\min}}^{t_{\max}} Q(t)\mathrm{d}t}\right]^{1/2} = \left[\frac{R_2}{R_0} - \left(\frac{R_1}{R_0}\right)^2\right]^{1/2}. \tag{34}$$

The frequency response of the fibre is obtained by computing the discrete Fourier transform of the discretized impulse response. More specifically, this is accomplished by implementing the fast Fourier transform (FFT) [65, 67, 68]. Finally, the fibre bandwidth is obtained from the frequency at half-maximum of the frequency response. Such a method leads to more accurate results than calculating the fibre bandwidth from the inverse of the rms pulse width (σ) assuming that the impulse response is Gaussian [69, 70].

The reader is again cautioned that the numerical results obtained from the computer simulations correspond only to ideal fibres, whereas in real fibres intrinsic physical phenomena can give rise to many different effects that can have an influence on the fibre transmission characteristics [52, 71–74]. It turns out that in real fibres there is always a certain amount of mode coupling which tends to increase the bandwidth and leads to a square-root dependence of the bandwidth on the fibre length, instead of the expected linear dependence without mode coupling [51, 69, 75–77]. In this sense, the numerical predictions can be regarded as a lower bound for the fibre bandwidth expected in practice [70].

4.2. Measurement of the impulse response and the fibre bandwidth

In order to accurately predict the fibre bandwidth, it is necessary to know the real numerical apertures of the fibres (the bandwidth increases when the fibre numerical aperture

© 2008 by WILEY-VCH Verlag GmbH & Co. KGaA, Weinheim

decreases). Nevertheless, the selection of any value for the fibre numerical aperture does not change the shape of the impulse response, since this one mainly depends on the refractive index profile rather than on the value of the fibre numerical aperture. In our calculations we have taken the typical characteristics of PMMA-based POFs with the highest possible fibre numerical aperture, so that the Eska-Miu and TVER MSI-POFs exhibit a peak numerical aperture (NA_f) of 0.51 (which is the worst case) [4]. Notice that, because of this high numerical aperture, we can safely neglect the effects of chromatic dispersion on fibre bandwidth [20].

We have employed a Lambertian source of radius r_s covering the whole input surface of the fibres and emitting light in all directions, i.e. with a source numerical aperture $NA_s = 1.0$. We have taken a straight section of 100 m in every case.

Fig. 14 shows the impulse response of the MSI-POFs considered above. The details of the rms pulse width (σ) and the fibre bandwidth (BW) are shown in Table 5.

It is clear from Table 5 that the influence of tunnelling rays on fibre bandwidth is slightly stronger in the case of the Eska-Miu fibre than in the case of the TVER one (the bandwidth reduction due to tunnelling rays is in the order of 15% in the Eska-Miu fibre and of 8% in the TVER one). This is consistent with the fact that there are relatively more tunnelling rays in the Eska-Miu fibre than in the TVER one, because the region of tunnelling rays on the $\tilde{\beta}$-$\tilde{l}$ plane is wider in the former case than in the latter. Therefore, it is expected that, in general, their effect on bandwidth will be slightly greater in the Eska-Miu fibre than in the TVER one.

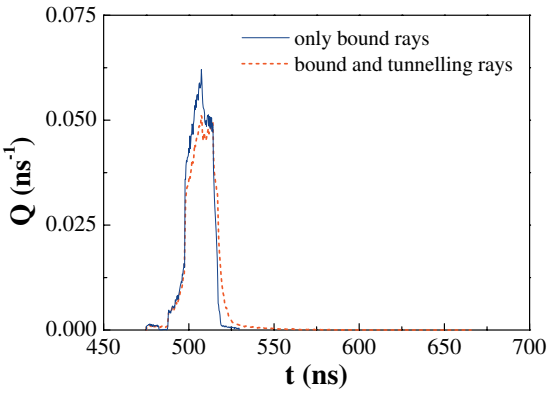

(a) Eska-Miu fibre.

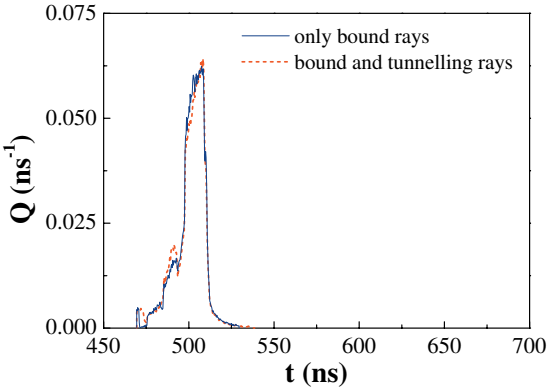

(b) TVER fibre.

Figure 14 (online color at: www.lpr-journal.org) Impulse response $Q(t)$ for the investigated MSI-POFs (the impulse responses are normalized so that they have unit total power).

Table 5 Results obtained for the rms pulse width (σ) measured in ns and for the fibre bandwidth (BW) measured in MHz for the Eska-Miu and TVER MSI-POFs.

	Only bound rays		Tunnelling and bound rays	
	σ	BW	σ	BW
Eska-Miu fibre	6.76	29.4	9.57	25.02
TVER fibre	8.38	26.45	9.19	24.41

In view of the obtained results, both MSI-POFs exhibit higher bandwidths than an SI-POF of similar characteristics (we would achieve ≈ 18 MHz if we used an SI fibre), but they are much lower than in the case of a clad-parabolic-profile GI-POF (with a bandwidth of several hundreds of MHz in 100 m).

Next, we will analyse the fibre bandwidth against different source parameters while maintaining the rest of the parameters fixed, for the Eska-Miu and TVER MSI-POFs.

The different source configurations considered in this study are:

- the source numerical aperture NA_s in the interval [0.1, 1.0],
- the source radius r_s/ρ_N in the interval [0.1, 1.0], and
- the offset of launch position $Offset/\rho_N$ in the interval [0.0, 1.0].

We have plotted the obtained results on Figs. 15 and 16. The step size for each set of measurements has been adjusted so that we have 100 samples in each figure. For the sake of clarity, only part of the line-symbols have been drawn.

From direct comparison between the aforementioned figures, it can be concluded that, in both MSI-POFs, a significant bandwidth improvement (a twenty-fold increase) can be obtained by reducing both the source numerical aperture (NA_s) and its normalized radius (r_s/ρ_N) to the common value of 0.1. Even though the effective solid acceptance angle of the fibre is sufficiently high to accept more tilted rays (due to its high numerical aperture), the rays launched under these conditions do not fill this effective solid acceptance angle. This fact leads to a reduction of the intermodal dispersion (i.e. the fibre bandwidth increases).

As for tunnelling rays, their effect is to decrease the fibre bandwidth, especially when large-diameter sources are involved, as is evident from Fig. 15.

The fact that the core of MSI fibres consists of several layers of different refractive indices has a strong effect

© 2008 by WILEY-VCH Verlag GmbH & Co. KGaA, Weinheim

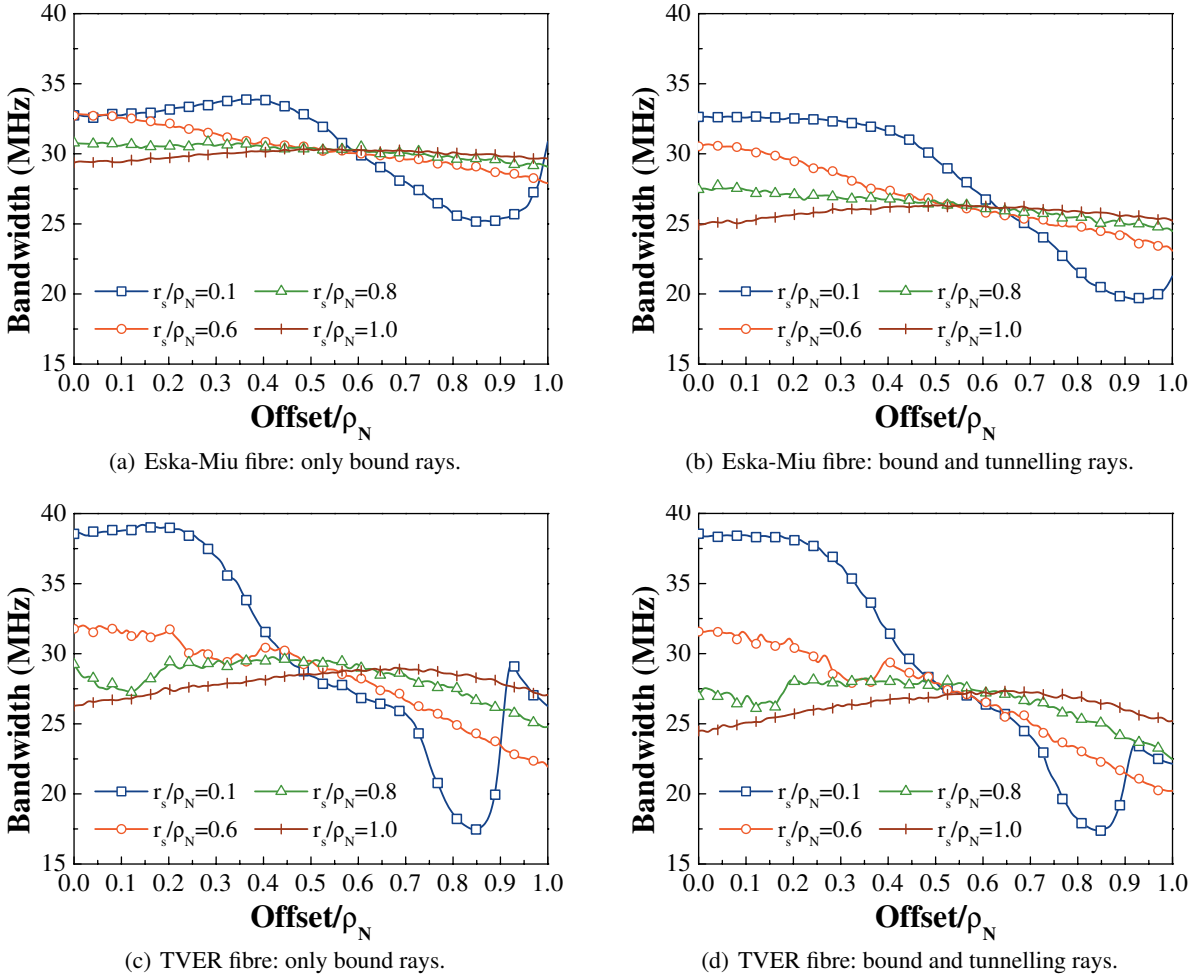

(a) Eska-Miu fibre: only bound rays.

(b) Eska-Miu fibre: bound and tunnelling rays.

(c) TVER fibre: only bound rays.

(d) TVER fibre: bound and tunnelling rays.

Figure 15 (online color at: www.lpr-journal.org) Fibre bandwidth against offset of launch position for various source radii.

on fibre bandwidth. For example, it can be observed from Fig. 15 that, if we consider small sources (say, $r_s/\rho_N = 0.1$), the transit times for bound rays will depend strongly on the position of the light source relative to the core centre ($Offset/\rho_N$). To put it another way, these transit times (and, consequently, the bandwidth) depend on the layer of the fibre on which these rays are launched (compare the degree of variability in the bandwidth when $r_s/\rho_N = 0.1$ with the results obtained when $r_s/\rho_N = 1.0$).

It is particularly interesting to note that the inflexion points, maxima and minima in the bandwidth curves for $r_s/\rho_N = 0.1$ correspond to those positions of the light source for which it starts or ceases to cover part of another layer of the fibre. For instance, in the case of the TVER fibre, it can be seen in both Figs. 15(c) and 15(d) that, from the offset of launch position $Offset/\rho_N = 0.92$, the bandwidth starts to decrease again after having increased in the interval $[0.82, 0.92]$. It turns out that 0.82 is the normalized radial limit between the third layer and the outermost one, i.e. $\rho_3/\rho_N = 0.82$ (refer back to Table 1 for further details), and also that the source only covers the outermost layer from the limit value of $Offset/\rho_N = 0.92$. However, in the case of the Eska-Miu fibre (see Figs. 15(a) and 15(b)), we have that the limit between the second layer and the outermost one is $\rho_2/\rho_N = 0.92$, so the light source will still cover part of the second layer in addition to the outermost one, even if the offset of launch position is maximum (i.e. $Offset/\rho_N = 1.0$) and, therefore, we will not be able to observe the same effects as with the TVER fibre.

In view of the previous facts, it is clear that the fibre bandwidth depends strongly on the fibre refractive index profile. This explains the differences observed in the results obtained for the Eska-Miu fibre and the TVER one.

Another interesting effect of the multilayered refractive index profile inherent to these fibres can be observed in Fig. 16, which shows the change in fibre bandwidth with the source numerical aperture for different source radii.

It is clear that the high bandwidth attainable with low values of NA_s is rapidly neutralized if the source covers additional layers. In the case of the Eska-Miu fibre (see Figs. 16(a) and 16(b)), we can observe that the highest bandwidths are obtained for small sources with $r_s/\rho_N = 0.1$

© 2008 by WILEY-VCH Verlag GmbH & Co. KGaA, Weinheim

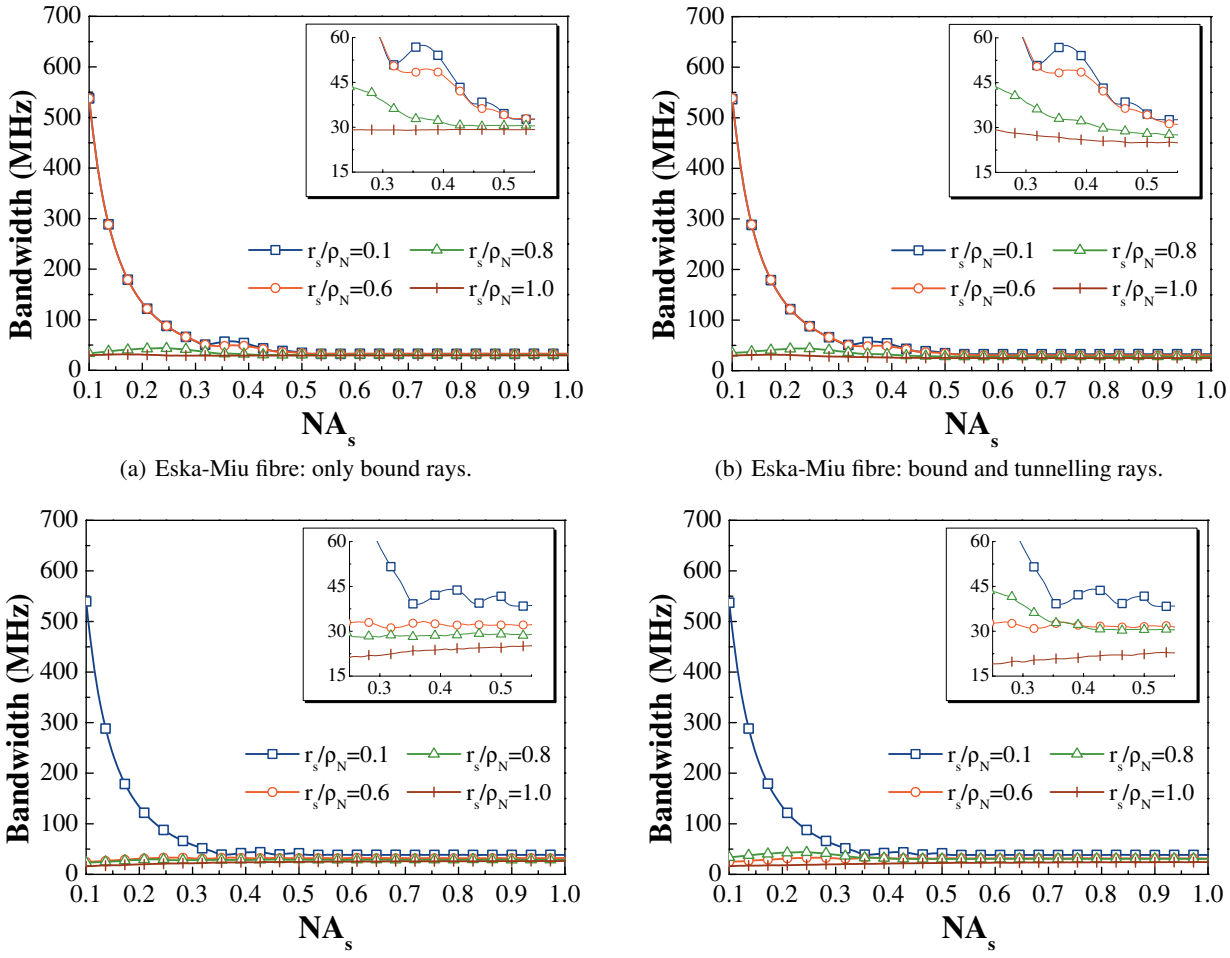

(a) Eska-Miu fibre: only bound rays.

(b) Eska-Miu fibre: bound and tunnelling rays.

(c) TVER fibre: only bound rays.

(d) TVER fibre: bound and tunnelling rays.

Figure 16 (online color at: www.lpr-journal.org) Fibre bandwidth against source numerical aperture for various source radii. The insets show a magnified view of the fibre bandwidth.

and 0.6 (i.e. when the source only covers the first layer considered here, since the radial limit value between the first and second layers is $\rho_1/\rho_N = 0.66$), whereas for $r_s/\rho_N = 0.8$ and 1.0 this bandwidth improvement is gradually spoilt. In the case of the TVER fibre, this limit value is lower ($\rho_1/\rho_N = 0.48$) and, as a consequence, we achieve these higher bandwidths only for $r_s/\rho_N = 0.1$, as can be deduced from Figs. 16(c) and 16(d). It turns out that the refractive index profile of MSI fibres plays a key role in this bandwidth worsening. When we cover the whole input surface of the fibre, even if we employ a restricted launching condition (namely, if NA_s is kept low), the rays excited on the innermost and outermost layers have very different transit times due to the difference in the refractive indices. This leads to an increase in the intermodal dispersion and, therefore, the fibre bandwidth reduces.

On the other hand, we can observe fluctuations or ripples in the fibre bandwidth that depend on the fibre refractive index profile when small sources are employed (the insets in Fig. 16 provide a clearer view of the variations). For instance, if we consider the case of $r_s/\rho_N = 0.1$, the tendency of the fibre bandwidth is to decrease as NA_s increases, since then more tilted rays are launched into the first layer and, consequently, the intermodal dispersion is higher. When a certain value of NA_s is exceeded (0.3 in the case of the Eska-Miu fibre and 0.33 in the case of the TVER one), the more tilted rays now pass to the second layer. These rays propagate faster in this layer because of its lower refractive index, which tends to equalize and even reduce the intermodal dispersion. For example, in the case of the Eska-Miu fibre, the decrease in the bandwidth is gradually compensated in the interval $[0.3, 0.32]$ (in the case of the TVER fibre in the interval $[0.33, 0.36]$), and even improved in the interval $[0.32, 0.36]$ (in the case of the TVER fibre in the interval $[0.36, 0.42]$). Nevertheless, if even more tilted rays are launched the fibre bandwidth tends to worsen again, since then the boost experienced by the rays propagating within the second layer does not compensate the extra length that they must travel. Such a worsening continues until rays can pass to the third layer,

© 2008 by WILEY-VCH Verlag GmbH & Co. KGaA, Weinheim

which occurs for values of NA_s exceeding the limit 0.45 in the case of the Eska-Miu fibre (with a slight improvement in the interval [0.45, 0.47]), and the limit 0.44 in the case of the TVER one (the improvement taking place in the interval [0.45, 0.5] instead). When NA_s increases further, the same phenomenon occurs again until rays are able to reach the outermost layer, even though the ripples observed in the fibre bandwidth tend to decrease as ray propagation takes place within more layers.

5. Conclusions

In this review we have carried out an extensive analysis of light propagation properties in MSI fibres based on classical geometric optics. After having derived the ray invariants, which allow us to determine exactly the ray trajectories inside these fibres, we have classified rays into bound, refracting and tunnelling categories. We have obtained a single theoretical expression for the calculation of the power transmission coefficient of tunnelling and refracting rays in MSI fibres. Tunnelling rays have a strong influence on the performance of MSI fibres, which depends on the fibre refractive index profile.

We have also obtained analytical expressions that allow us to calculate both the extrinsic and intrinsic coupling losses in MSI fibres. In all cases, the formulae were derived on the assumption that the power distribution is uniform across the light cone of radiation defined by the input numerical aperture. For this reason, the analytical calculations performed overestimate the attenuation, providing an upper bound for coupling losses. This property ensures that measurements obtained in practice will always be well below these limit values. As for extrinsic coupling losses, the results yielded by the numerical computer simulations have revealed that the transverse offset is the most critical parameter. Concerning intrinsic coupling losses, reducing the variations in the numerical aperture and the core diameter helps to minimize these losses.

Additionally, we have carried out a numerical analysis of the pulse dispersion and bandwidth in MSI fibres under different light source configurations, taking into account the influence of tunnelling rays. The obtained results have revealed, on the one hand, variations in fibre bandwidth as a direct consequence of the multilayered refractive index profile inherent to these fibres, and, on the other hand, a higher sensitivity of the fibre bandwidth to the offset of launch position when the source is made smaller.

Acknowledgements The authors would like to thank Prof. H. Poisel of the University of Applied Sciences of Nuremberg for many fruitful discussions.

This work was supported by the institutions *Ministerio de Educación y Ciencia*, *Universidad del País Vasco/Euskal Herriko Unibertsitatea*, *Gobierno Vasco/Eusko Jaurlaritza*, and *European Union 7th Research Framework Programme*, under projects TEC2006-13273-C03-01, GIU05/03 and EJIE07/12, SAIOTEK'07, and AISHA2, respectively.

Joseba Zubia received the M. Sc. degree in solid-state physics and the Ph. D. degree in physics from the University of the Basque Country, Bilbao, Spain, in 1988 and 1993, respectively. His Ph. D. work focused on the optical properties of ferroelectric liquid crystals.

He is currently a Full Professor with the Department of Electronics and Telecommunications, School of Engineering of Bilbao, University of the Basque Country. He has more than 12 years of experience doing basic research in the field of polymer optical fibres and is currently involved in research projects in collaboration with universities and companies from Spain and other countries in the field of polymer optical fibres, fibre-optic sensors, and liquid crystals.

Prof. Zubia was a recipient of a special award for Best Thesis in 1995.

Gotzon Aldabaldetreku received the M. Sc. degree and the Ph. D. degree in telecommunications engineering from the University of the Basque Country, Bilbao, Spain, in 2000 and 2006, respectively. His Ph. D. work focused on the theoretical analysis of light propagation properties in multimode multi-step index optical fibres.

For nearly seven years, he has been doing research on optical fibres at the Department of Electronics and Telecommunications, School of Engineering of Bilbao, University of the Basque Country, where he became an Assistant Lecturer in 2002.

Dr. Aldabaldetreku was a recipient of a European acknowledgement of the Ph. D. degree.

Gaizka Durana received the M. Sc. degree in solid-state physics from the University of the Basque Country, Bilbao, Spain, in 1999. He is currently working toward the Ph. D. degree in the study of light polarization properties in polymer optical fibres at the University of the Basque Country.

He is currently a Lecturer and a Researcher with the Department of Electronics and Telecommunications, School of Engineering of Bilbao, University of the Basque Country.

© 2008 by WILEY-VCH Verlag GmbH & Co. KGaA, Weinheim

Jon Arrue received the M. Sc. degree in electronic physics, completed a 12-month postgraduate course in electronics and a 12-month postgraduate course in telecommunications, and received the Ph. D. degree in optical fibres from the University of the Basque Country, Bilbao, Spain, in 1990, 1991, 1992, and 2001, respectively.

He is currently a Professor with the Department of Electronics and Telecommunications, School of Engineering of Bilbao, University of the Basque Country, and is also involved in international research projects with other universities and companies.

Dr. Arrue was a recipient of a special award for his thesis and a European acknowledgement of the Ph. D. degree.

Felipe Jiménez received the M. Sc. degree and the Ph. D. degree in Industrial Engineering from the University of the Basque Country, Bilbao, Spain, in 1990 and 2000 respectively, with a doctorate dissertation in the field of Geometric Design.

He is currently an Associate Professor with the Department of Applied Mathematics , School of Engineering of Bilbao, University of the Basque Country, teaching Numerical Methods. He is also an active member of its Applied Photonics research group, where his contribution specializes on the numerical simulation of light propagation in plastic optical fibres.

References

[1] J. P. Powers, An introduction to fiber optics systems, 2 edition (McGraw-Hill, United States of America, 1993).

[2] G. E. Agrawal, Fiber-optic communication systems, 3 edition (John Wiley & Sons, New York, 2002).

[3] T. Kaino, Polymer optical fibers, in: Polymers for lightwave and integrated optics, edited by L. A. Hornak (Marcel Dekker, Inc., New York, 1992), Chap. 1.

[4] J. Zubia and J. Arrue, Opt. Fiber Technol. **7**(2), 101–140 (2001).

[5] W. Daum, J. Krauser, P. E. Zamzow, and O. Ziemann, POF: Polymer optical fibers for data communication (Springer, Berlin, 2002).

[6] Y. Koike, E. Nihei, N. Tanio, and Y. Ohtsuka, Appl. Opt. **29**(18), 2686–2691 (1990).

[7] Y. Koike, POLYMER **32**(10), 1737–1745 (1991).

[8] Y. Ohtsuka, E. Nihei, and Y. Koike, Appl. Phys. Lett. **57**(2), 120–122 (1990).

[9] H. Murofushi, Low loss perfluorinated POF, in: Proceedings of the fifth international conference on plastic optical fibres and applications-POF'96, (Paris (France), 1996), pp. 17–23.

[10] Asahi Gass Co., Ltd.: Lucina™. http://www.agc.co.jp/lucina/index.htm.

[11] Giga House Town. http://www.ght.jp.

[12] Mitsubishi Rayon Co., Ltd.: Eska-Miu. http://www.pofeska.com.

[13] V. Levin, T. Baskakova, Z. Lavrova, A. Zubkov, H. Poisel, and K. Klein, Production of multilayer polymer optical fibers, in: Proceedings of the eighth international conference on plastic optical fibers and applications-POF'99, (Chiba (Japan), July 1999), pp. 98–101.

[14] K. Irie, Y. Uozu, and T. Yoshimura, Structure design and analysis of broadband POF, in: Proceedings of the tenth international conference on plastic optical fibers and applications-POF'01, (Amsterdam (The Netherlands), September 2001), pp. 73–79.

[15] S. Lee, L. C. Paek, and Y. Chung, Microwave Opt. Technol. Lett. **39**(2), 129–131 (2003).

[16] G. Aldabaldetreku, G. Durana, J. Zubia, J. Arrue, H. Poisel, and M. A. Losada, Opt. Express **13**(11), 4012–4036 (2005).

[17] G. Aldabaldetreku, G. Durana, J. Zubia, J. Arrue, F. Jiménez, and J. Mateo, Opt. Express **13**(9), 3283–3295 (2005).

[18] G. Aldabaldetreku, G. Durana, J. Zubia, and J. Arrue, J. Lightwave Technol. **24**(3), 1364–1375 (2006).

[19] M. Born and E. Wolf, Principles of optics, 6 edition (Pergamon Press, New York, 1990).

[20] A. W. Snyder and J. D. Love, Optical waveguide theory (Chapman and Hall, London, 1983).

[21] R. J. Pieper and A. Nassopoulos, IEEE Trans. Educ. **40**(2), 139–143 (1997).

[22] D. Gloge and E. A. J. Marcatili, Bell Syst. Tech. J. **52**, 1563–1578 (1973).

[23] A. Ankiewicz, Geometric optics theory of graded index optical fibres, PhD thesis, Australian National University, 1978.

[24] D. Marcuse, D. Gloge, and E. A. J. Marcatili, Guiding properties of fibers, in: Optical fiber telecommunications, edited by S. E. Miller and A. G. Chynoweth (Academic Press, Inc., San Diego, California, 1979), Chap. 3.

[25] R. Sammut and A. W. Snyder, Appl. Opt. **15**(2), 477–482 (1976).

[26] G. Aldabaldetreku, J. Zubia, G. Durana, and J. Arrue, Opt. Express **14**(4), 1413–1429 (2006).

[27] A. W. Snyder and J. D. Love, Opt. Commun. **12**(3), 326–328 (1974).

[28] J. D. Love and C. Winkler, J. Opt. Soc. Am. **67**(12), 1627–1632 (1977).

[29] S. Zhu, A. W. Yu, D. Hawley, and R. Roy, Am. J. Phys. **54**(7), 601–606 (1986).

[30] F. P. Zanella, D. V. Magalhães, M. M. Oliveira, R. F. Bianchi, L. Misoguti, and C. R. Mendonça, Am. J. Phys. **71**(5), 494–496 (2003).

[31] A. A. Stahlhofen, Am. J. Phys. **72**(3), 412 (2004).

[32] O. Bryngdahl, Evanescent waves in optical imaging, in: Progress in optics XI, edited by E. Wolf (North-Holland, Amsterdam, 1973), Chap. 4.

© 2008 by WILEY-VCH Verlag GmbH & Co. KGaA, Weinheim

[33] R. J. Black and A. Ankiewicz, Am. J. Phys. **53**(6), 554–563 (1985).
[34] A. W. Snyder, D. J. Mitchell, and C. Pask, J. Opt. Soc. Am. **64**(5), 608–614 (1974).
[35] A. W. Snyder and D. J. Mitchell, J. Opt. Soc. Am. **64**(5), 599–607 (1974).
[36] J. D. Love and C. Winkler, Appl. Opt. **17**(14), 2205–2208 (1978).
[37] A. W. Snyder and D. J. Mitchell, Optik **40**(4), 438–459 (1974).
[38] A. W. Snyder and J. D. Love, IEEE Trans. Microwave Theory Tech. **23**(1), 134–141 (1975).
[39] J. D. Love and C. Winkler, IEEE Trans. Microwave Theory Tech. **28**(7), 689–695 (1980).
[40] J. D. Love and C. Winkler, Opt. Quantum Electron. **10**(4), 341–351 (1978).
[41] M. Abramowitz and I. A. Stegun, Handbook of mathematical functions with formulas, graphs, and mathematical tables (Dover Publications, Inc., New York, 1965).
[42] D. Marcuse, in: Principles of optical fiber measurements (Academic Press, Inc., London, 1981), Chap. 4.
[43] Japanese Standards Association, Test methods for structural parameters of all plastic multimode optical fibers, Tech. Rep. JIS C 6862, JIS, Tokyo, Japan, 1990.
[44] D. Gloge, Bell Syst. Tech. J. **55**(7), 905–916 (1976).
[45] T. C. Chu and A. R. McCormick, Bell Syst. Tech. J. **57**(3), 595–602 (1978).
[46] F. L. Thiel and R. M. Hawk, Appl. Opt. **15**(11), 2785–2791 (1976).
[47] G. Keiser, Optical fiber communications (McGraw-Hill, Singapore, 1991).
[48] J. M. Senior, in: Optical fiber communications: Principles and practice (Prentice Hall, London, 1985), Chap. 5.
[49] J. P. Powers, in: An introduction to fiber optics systems, 2 edition (McGraw-Hill, United States of America, 1993), Chap. 4.
[50] R. Olshansky and S. M. Oaks, Appl. Opt. **17**(11), 1830–1835 (1978).
[51] G. Jiang, R. F. Shi, and A. F. Garito, IEEE Photon. Technol. Lett. **9**(8), 1128–1131 (1997).
[52] T. Ishigure, M. Kano, and Y. Koike, J. Lightwave Technol. **18**(7), 959–965 (2000).
[53] S. E. Golowich, W. R. White, W. A. Reed, and E. Knudsen, J. Lightwave Technol. **21**(1), 111–121 (2003).
[54] S. Savović and A. Djordjevich, Appl. Opt. **41**(36), 7588–7591 (2002).
[55] S. Savović and A. Djordjevich, Appl. Opt. **43**(29), 5542–5546 (2004).
[56] F. L. Thiel and D. H. Davis, Electron. Lett. **12**(13), 340–341 (1976).
[57] D. J. Bond and P. Hensel, Opt. Quantum Electron. **13**(1), 11–18 (1981).
[58] J. Zubia, G. Aldabaldetreku, G. Durana, J. Arrue, C. A. Bunge, and H. Poisel, Fiber Integr. Opt. **23**(2/3), 121–156 (2004).
[59] K. F. Barrell and C. Pask, Appl. Opt. **19**(8), 1298–1305 (1980).
[60] A. W. Snyder, D. J. Mitchell, and C. Pask, Electron. Lett. **11**(13), 275–277 (1975).
[61] A. W. Snyder, Appl. Opt. **15**(5), 1290–1294 (1976).
[62] F. Albertin, P. D. Vita, and R. Vannucci, Opto-electronics **6**(5), 369–386 (1974).
[63] A. Ankiewicz and C. Pask, Opt. Quantum Electron. **9**(2), 87–109 (1977).
[64] A. Ankiewicz and C. Pask, Opt. Quantum Electron. **15**(6), 463–470 (1983).
[65] W. H. Press, B. P. Flannery, S. A. Teukolsky, and W. T. Vetterling, Numerical recipes in C: The art of scientific computing (Cambridge University Press, Cambridge, 2002).
[66] D. Marcuse, Appl. Opt. **18**(12), 2073–2080 (1979).
[67] A. V. Oppenheim, R. W. Schafer, and J. R. Buck, in: Discrete-time signal processing, 2 edition (Prentice Hall, London, 1999), Chap. 9.
[68] J. G. Proakis and D. G. Manolakis, in: Digital Signal Processing. Principles, algorithms, and applications, 3 edition (Prentice Hall, London, 1997), Chap. 6.
[69] C. Koeppen, R. F. Shi, W. D. Chen, and A. F. Garito, J. Opt. Soc. Am. B **15**(2), 727–739 (1998).
[70] H. M. Presby, D. Marcuse, and L. G. Cohen, Appl. Opt. **18**(19), 3249–3255 (1979).
[71] D. Gloge, Bell Syst. Tech. J. **51**, 1767–1783 (1972).
[72] D. Marcuse, Bell Syst. Tech. J. **51**(1), 229–237 (1972).
[73] W. A. Gambling, D. N. Payne, and H. Matsumura, Appl. Opt. **14**(7), 1538–1542 (1975).
[74] R. Olshansky, Appl. Opt. **14**(4), 935–945 (1975).
[75] D. Gloge, Bell Syst. Tech. J. **52**, 801–816 (1973).
[76] S. D. Personick, Bell Syst. Tech. J. **50**(3), 843–859 (1971).
[77] M. Miyamoto, R. Yamauchi, and K. Inada, J. Lightwave Technol. **LT-1**(2), 463–470 (1983).

© 2008 by WILEY-VCH Verlag GmbH & Co. KGaA, Weinheim